

# **LEGIBILITY NOTICE**

A major purpose of the Technical Information Center is to provide the broadest dissemination possible of information contained in DOE's Research and Development Reports to business, industry, the academic community, and federal, state and local governments.

Although a small portion of this report is not reproducible, it is being made available to expedite the availability of information on the research discussed herein.

Received by C

JUN 07 1989

Los Alamos National Laboratory is operated by the University of California for the United States Department of Energy under contract W 7405-ENG 36

LA-UR--89-1604

DE89 012617

TITLE MOMENTUM DISTRIBUTIONS: AN OVERVIEW

AUTHOR(S) P. E. Sokol\*  
R. N. Silver, T-11/LANSCE  
J. W. Clark\*\*

SUBMITTED TO Plenum Press

\*Department of Physics  
The Pennsylvania State University  
University Park, PA 16802

\*\*McDonnell Center for the Space Sciences  
and Department of Physics  
Washington University  
St. Louis, MO 63130

DISCLAIMER

This report was prepared as an account of work sponsored by an agency of the United States Government. Neither the United States Government nor any agency thereof, nor any of their employees, makes any warranty, express or implied, or assumes any legal liability or responsibility for the accuracy, completeness, or usefulness of any information, apparatus, product, or process disclosed, or represents that its use would not infringe privately owned rights. Reference herein to any specific commercial product, process, or service by trade name, trademark, manufacturer, or otherwise does not necessarily constitute or imply its endorsement, recommendation, or favoring by the United States Government or any agency thereof. The views and opinions of authors expressed herein do not necessarily state or reflect those of the United States Government or any agency thereof.

Reproduction of this report by the publisher recognizes that the U.S. Government retains a non-exclusive, royalty-free license to publish or reproduce the copyrighted material contained herein for government purposes.

Los Alamos National Laboratory requests that the publisher identify the article as work performed under the auspices of the U.S. Department of Energy.

Los Alamos National Laboratory  
Los Alamos, New Mexico 87545

DISTRIBUTION OF THIS DOCUMENT IS UNLIMITED

MR

## MOMENTUM DISTRIBUTIONS: AN OVERVIEW

P. E. Sokol  
Department of Physics  
The Pennsylvania State University  
University Park, PA 16802.

R. N. Silver  
MS B262 Theoretical Division  
Los Alamos Neutron Scattering Center  
Los Alamos National Laboratory  
Los Alamos, New Mexico 87545

J. W. Clark  
McDonnell Center for the Space Sciences  
and Department of Physics  
Washington University  
St. Louis, MO 63130

## INTRODUCTION

While all systems of classical particles have single-particle momentum distributions  $n(p)$  of Maxwell-Boltzmann form, the momentum distribution plays a role central to our understanding of systems of quantum particles. An outstanding example is the low-temperature superfluid behavior of the Bose liquid,  $^4\text{He}$ , where the superfluidity is associated with Bose condensation of a macroscopic fraction of the  $^4\text{He}$  atoms into a zero-momentum state. The momentum distribution is complementary to other characterizations of many-body systems and can be more informative. The pair correlation function of liquid  $^4\text{He}$  is very close to that of a hard-sphere classical fluid, whereas the momentum distribution reveals the quantum behavior in the form of a  $\delta$ -function spike in  $n(p)$  at  $p = 0$  due to the Bose condensate. Momentum distributions are equally fundamental to the description of Fermi systems. The Fermi-liquid properties of  $^3\text{He}$  and electrons in metals are associated with a discontinuity in the momentum distribution at the Fermi momentum,  $k_F$ , which defines a Fermi surface for a three-dimensional system. A detailed description of the, often complex, Fermi surfaces in metals is essential to understanding their transport, optical, and magnetic properties. At low temperatures, the transition to superfluid behavior of  $^3\text{He}$  and the transition to superconducting behavior of electrons is associated with the disappearance of this Fermi surface. An outstanding problem in nuclear physics is how the quasi-exponential high- $p$  tails observed in the  $n(p)$  of nucleons in nuclei are related to the short-range real-space correlations of nucleons due to the strongly repulsive core of the nucleon-nucleon potential. The momentum distributions of quarks are found to be different inside nuclei and inside free nucleons, which suggests a possible role for quarks in the description of nuclear forces. These varied illustrations attest to the importance of the momentum distribution as a revealing probe of the wave functions of quantum many-body systems.

Momentum distributions are of interest for most of the subjects of research in modern physics, including: systems of atoms, in solid and liquid phases; interacting electron systems, such as conduction electrons in metals; systems of nucleons in atomic nuclei and nuclear matter; and systems of quarks in high energy physics. We

across this diverse range of energy and length scales, forces, and system types. The general features of  $n(p)$  for systems of given statistics are in principle quite similar. In practice, theorists in the various areas of physics face similar problems when they attempt to predict the momentum distribution accurately, and experimentalists face similar problems when they make measurements of quantities related to the momentum distribution and attempt to extract  $n(p)$  from their data. In all fields there has been a rapid advance in theory and experiment (in particular, the development of large-scale facilities for scattering experiments), which is presenting exciting new scientific opportunities.

There have been several excellent reviews of momentum-distribution research in particular subject areas of physics such as electronic systems<sup>1</sup> and nuclear systems.<sup>2</sup> However, it is the commonality of interests, difficulties, and prospects across all of physics, along with certain pivotal advances, which led to the organization of an interdisciplinary Workshop on Momentum Distributions held at Argonne National Laboratory on October 24-26, 1988. The purpose of this overview is to explain why scientists with such diverse backgrounds have been brought together at this meeting, to introduce and discuss the common elements of momentum-distribution studies, and to establish a common language. We hope to facilitate an appreciation of the more specialized articles which follow in these proceedings.

We begin by summarizing the general properties of momentum distributions. Differences and similarities of atomic, electronic, and nuclear many-body systems are examined, in terms of characteristic lengths and energies, relative importance of exchange, and the nature of the two-particle interactions. We continue with a brief commentary on the microscopic methods used to calculate  $n(p)$  from first principles. Thereafter the discussion focuses on the ideas, techniques, and issues involved in the experimental determination of the momentum distribution: deep-inelastic scattering, the impulse approximation,  $Y$ -scaling, final-state effects, and scale breaking. Finally, some typical examples of theoretical and experimental momentum distributions will be presented and compared, for a variety of systems.

## FUNDAMENTALS

The momentum distribution  $n(p)$  of a quantum-mechanical system is the average number of particles with momentum  $p$ , determined by the expectation value

$$n(p) = \langle \Psi | \sum_{\sigma} a_{p\sigma}^{\dagger} a_{p\sigma} | \Psi \rangle \quad (2.1)$$

In this expression,  $|\Psi\rangle$  is the unit-normalized  $N$ -particle state of the system and  $a_{p\sigma}^{\dagger}$  and  $a_{p\sigma}$  are creation and annihilation operators for a particle with momenta  $p$  and spin projection  $\sigma$ . Usually, one deals with the momentum distribution of particles having a given spin projection, defined by removing the spin sum in eq (2.1). At finite temperatures, Eq. (2.1) is replaced by an ensemble average over all  $N$ -particle states.

In the quantum systems of interest to us, the de Broglie wavelength for single-particle motion can be of the order of the interparticle spacing and in some cases much larger. This implies large exchange effects. The type of quantum statistics obeyed by the particles, Bose or Fermi, then has an important bearing on the character of the momentum distribution. For Bose particles, the many-body wave function must be symmetric and there is no restriction on the occupancy of any given one-body momentum state. For Fermi particles, the overall wave function must be antisymmetric. Consequently, the occupancy of any chosen one-body momentum state cannot be greater than one.

The behavior of non-interacting Bose and Fermi gases as the temperature is decreased from very high to very low values, or equivalently as the density is increased,

approaches a Gaussian, the classical Maxwell-Boltzmann form, and the occupancy of any particular momentum state is always much less than one. In this limit, the width of the momentum distribution is proportional to the thermal energy of the particles and the mean kinetic energy is  $3k_B T/2$ .

Upon lowering the temperature (or increasing the density), the occupancy of some of the one-body momentum states begins to approach one and the effects of statistics begin to emerge. The momentum distributions begin to deviate from the Maxwell-Boltzmann form. For non-interacting particles where the single-particle motion can be described by states of definite momentum, the symmetry requirement for Bose particles leads to the familiar Bose-Einstein momentum distribution, while the antisymmetry requirement for Fermi particles leads to the familiar Fermi-Dirac distribution.

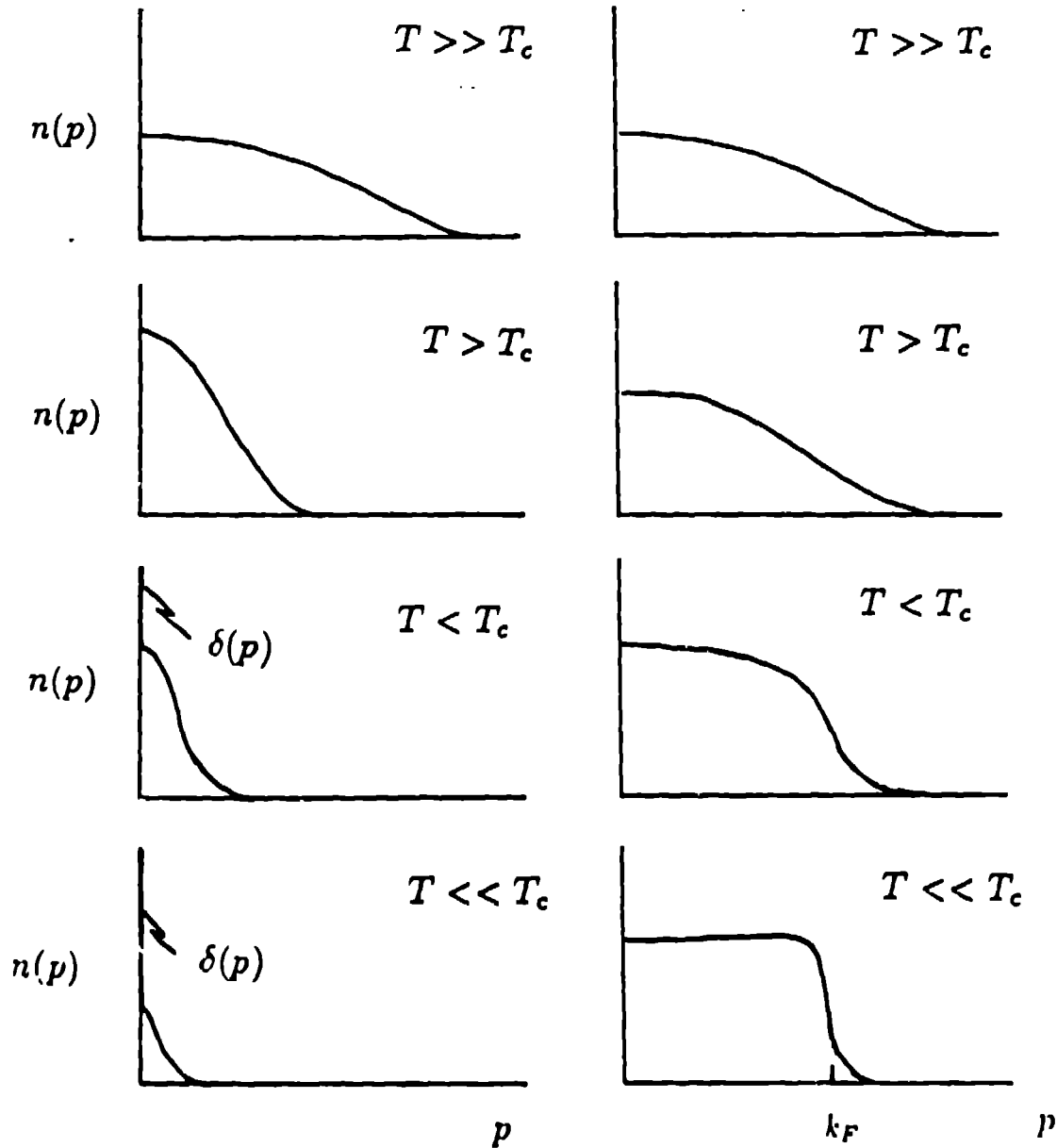


Fig. 1 Typical behavior of the momentum distribution as a function of temperature for the ideal Bose and Fermi gasses. The characteristic temperature  $T_c$  is defined in the text.

as the particles take advantage of the lack of any restriction on multiple occupation. The behavior in the Fermi case is quite different. The distribution remains flat and close to one in the small- $p$  region as the temperature is lowered, as if there were a repulsion between particles trying to pile up at the same momentum. This behavior is a direct consequence of the exclusion principle which forbids multiple occupation of a particular momentum state.

The effects of quantum statistics become dominant below a characteristic temperature,  $T_c$ . For both Fermi and Bose systems, we may define such a characteristic temperature by the condition that the thermal de Broglie wavelength of the particles is equal to some appropriate measure of the mean interparticle spacing.

The characteristic temperature for a Bose gas may be taken as the Bose-Einstein condensation temperature  $T_c = T_{BE} = (2\pi\hbar^2/1.897mk_B)\rho^{2/3}$ , where  $\rho$  is the density of the gas,  $m$  is the particle mass and  $k_B$  is Boltzmann's constant. At temperatures higher than  $T_{BE}$ , the occupancy of any particular one-body momentum state remains finite. Below this temperature, a macroscopic (i.e. of order the total number of particles in the system,  $N$ ) occupation of the  $k = 0$  momentum state develops, which is called "Bose-Einstein condensation." This is reflected in the appearance of a term in  $n(p)$  proportional to a Dirac delta function  $\delta(p)$ , with a coefficient which determines the (finite) fraction of particles residing in the Bose condensate. The condensate fraction increases as the temperature is lowered further until finally, at  $T = 0$ , all of the particles are in the condensate. The condensate particles occupy a single quantum state with a well defined momentum, namely  $p = 0$ . Bose condensation represents a novel macroscopic manifestation of quantum principles.

The characteristic temperature for a Fermi gas is determined by the Fermi energy. By definition this is the energy of the highest single-particle level occupied at  $T = 0$ , all of the lower levels each being filled with  $\nu$  particles, where  $\nu$  is the single-particle level degeneracy arising from spin (and possibly isospin) degrees of freedom. Thus  $T_c = T_F = (\hbar^2/2mk_B)(6\pi^2\rho/\nu)^{2/3}$ . As the temperature and hence the available thermal energy declines, the particles attempt to reduce their energies by occupying lower energy levels, but their readjustments are constrained by the exclusion principle. When the temperature has dropped substantially below  $T_c$  (say to  $T_c/5$  or  $T_c/10$ ), the lowest-lying single-particle levels will be completely filled with their retinue of fermions and  $n(p)$  will approach one. However, levels near the Fermi surface defined by  $k = k_F = (6\pi^2\rho/\nu)^{1/3}$  will be only partially occupied because of thermal excitation. The momentum distribution then exhibits the characteristic Fermi-Dirac shape, as shown in Fig. 1. With further decrease in temperature, the fall-off near the Fermi wave number  $k_F$  steepens until, at  $T = 0$ , all the particles have condensed into the "Fermi sea." The sharp discontinuity that appears in  $n(p)$  divides the momentum states below  $k_F$ , which are fully occupied, from those above, which are empty.

At  $T = 0$  in non-interacting systems, the fraction of Bose particles which are in the zero-momentum state reaches one, and there is a discontinuity of the Fermi  $n(p)$  at  $k_F$  equal to one. In interacting systems at  $T = 0$ , the features of macroscopic condensation at  $p = 0$  in Bose systems and a finite discontinuity at  $k_F$  in Fermi systems are predicted to persist under rather general assumptions. However, due to the interactions, the fraction of Bose particles which condense is less than one, and, for Fermi particles, the discontinuity at  $k_F$  takes some value less than one. These "depletion" effects will be discussed more fully below.

The single-particle properties of many-body systems, both interacting and non-interacting, may also be fruitfully discussed in terms of the one-body density matrix. For a unit-normalized pure quantum state, this quantity is defined by

$$\rho_1(r_1, r'_1) = N \int dr_2 \dots dr_N \Psi^*(r_1 r_2 \dots r_N) \Psi(r'_1 r_2 \dots r_N) \quad (2.2)$$

where spin and other internal degrees of freedom have been suppressed for simplicity.

The pair function  $\rho_1(r_1, r_1')$  measures the change of the wave function as a single particle is moved from  $r_1$  to  $r_1'$ , all the other particles remaining fixed. In general, the one-body density matrix will depend on  $r_1$  and  $r_1'$  individually. However, in a homogeneous, isotropic fluid it can only depend on the magnitude of the separation vector:

$$\rho_1(r_1, r_1') = \rho_1(|r_1 - r_1'|) \quad (2.3)$$

The single-particle density matrix of the fluid contains all the features of interest for this overview; hence we shall restrict our attention to that case.

The momentum distribution and the one-body density matrix are related by Fourier transformation. For a Fermi system, we may write simply

$$n(p) = \nu^{-1} \int \rho_1(r) e^{ipr} dr \quad (2.4)$$

where  $\nu$  is the level degeneracy. For a Bose system, the momentum distribution is traditionally separated into two components, a delta function term representing the zero-momentum condensate and a smooth component corresponding to occupation of the other single-particle states. Thus

$$n(p) = (2\pi)^3 \rho n_0 \delta(p) + n'(p) \quad (2.5)$$

where the condensate fraction is determined by

$$n_0 = \lim_{r \rightarrow \infty} \rho_1(r) / \rho \quad (2.6)$$

and the non-condensate portion has the Fourier representation

$$n'(p) = \int [\rho_1(r) - \rho_1(\infty)] e^{ipr} dr \quad (2.7)$$

Typical behaviors of both  $n(p)$  and  $\rho(r)$  for interacting Bose and Fermi systems at zero temperature are indicated in Fig. 2. To be definite, the particles are assumed to experience strong repulsive two-body interactions at small separations.

Consider first the one-body density matrix and momentum distribution of the ground state of the interacting Bose system. The dynamical short-range correlations due to the core repulsion, which govern the small- $r$  behavior of  $\rho_1(r)$  without regard to statistics, determine  $n(p)$  at large  $p$ . The effects of statistical correlations are most apparent in  $\rho_1(r)$  at large  $r$  and in  $n(p)$  at small  $p$ . The condensate, which gives rise to a finite value of  $\rho_1(r)$  at infinity, again manifests itself in  $n(p)$  as a delta-function spike at  $p = 0$  (not visible in the plot). The detailed behavior of both quantities at intermediate  $r$ , or  $p$ , is also significantly affected by the statistics. An interesting singular feature of the uncondensed component at small  $p$  results from the coupling of long-wavelength density fluctuations to the condensate. This feature leads to a finite intercept of  $pn(p)$  at  $p = 0$ , as shown<sup>3</sup> in Fig. 2.

Now consider the ground-state momentum distribution of the interacting Fermi system, as sketched in Fig. 2. The step function  $\theta(p - k_F)$  which gives  $n(p)$  for the noninteracting Fermi gas is modified in the presence of interactions, but the general shape is preserved. The interactions promote some of the particles from single-particle states inside the Fermi sea, i.e., with momenta less than  $k_F$ , to states outside, thus depleting the Fermi sea and creating a tail at higher momenta. If the system remains "normal," meaning that the interactions are not such as to create a superfluid ground state,  $n(p)$  retains its most characteristic Fermi feature, namely a discontinuity at the Fermi wave number (cf. Fig. 2). The size of the discontinuity, denoted herein

measure of the strength of the interparticle coupling.

Since the type of statistics has little effect on  $\rho_1(r)$  at small  $r$ , the one-body density matrix for the Fermi system is similar to that for the Bose system in that region, as seen in Fig. 2. However, at large  $r$  the behavior of this quantity is markedly different in the two systems: whereas the Bose  $\rho_1(r)$  approaches a constant value, reflecting the existence of a condensate and therefore off-diagonal long-range order<sup>4,5</sup> (ODLRO), the Fermi  $\rho_1(r)$  damps out to zero, in accordance with the absence of ODLRO at the one-particle level. The oscillatory behavior of the Fermi  $\rho_1(r)$  is required to produce the discontinuity of  $n(p)$  at  $k_F$ . The zeros of  $\rho_1(r)$  are determined by the location of the Fermi surface, and the overall amplitude of the oscillations is determined by the magnitude of  $Z_{k_F}$ .

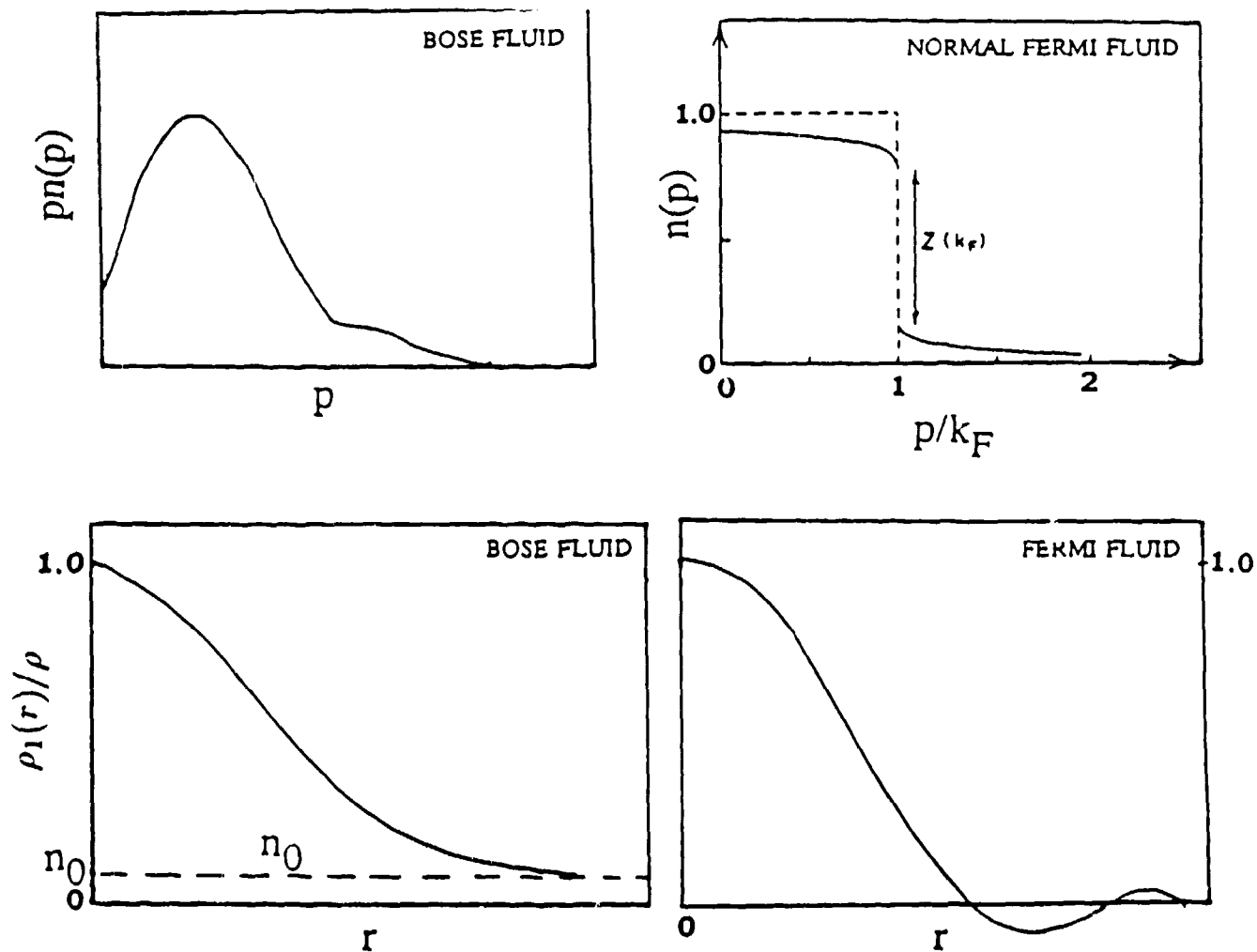


Fig. 2 Typical behavior of the momentum distribution and one-body density matrix in the ground state for interacting Bose and Fermi systems.

## SCALES

Before proceeding to more concrete matters of calculation and measurement, it will be useful to formulate meaningful bases for comparison of the diverse many-body systems involved in our studies. In so doing we shall gain a better understanding of their similarities and differences and begin to establish a common language for the subsequent discussions.

Our overview will focus on three types of many-body systems. It will be convenient to refer to collections of atoms, like liquid or solid  $^4\text{He}$  or  $^3\text{He}$  or solid molecular hydrogen, simply as *atomic systems*. By *nuclear systems* we shall mean both



more nuclei and idealized, infinite nuclear matter. The third category, *electronic systems*, includes, narrowly, the system of electrons in a solid, and, more broadly, a wide variety of systems of great topical interest in condensed-matter physics (e.g. in high-temperature superconductivity). Other many-body systems could also be considered, such as collections of quarks in particle physics, and collections of electrons in atoms and molecules. Although lack of space prevents us from doing justice to these additional examples, the concepts we shall discuss are generally applicable to all momentum-distribution studies.

A length scale appropriate to microscopic description of a given many-body system may be taken as a typical interparticle spacing, while the binding energy per particle provides a reasonable energy scale. The three classes of many-body problems we have just delineated involve very different scales in energy and length, ranging over many orders of magnitude. To make a meaningful comparison of system properties and behavior, we need somehow to remove these large variations.

We begin by considering condensed systems of atoms: solids and liquids. A typical interparticle spacing for atomic systems is on the order of  $\text{\AA}$ , setting the characteristic length scale. Typical binding energies for atomic systems are on the order of meV, setting the characteristic energy scale. Numerical values are shown in Table I for  $^3\text{He}$ , a "representative" atomic system.

Focusing on Fermi examples, how important are exchange effects in determining the shape of the momentum distribution? A measure of the strength of exchange, or statistical correlations, is given by the Fermi energy  $E_F$  of the system. If  $E_F$  is large compared to the binding energy per particle,  $E_b$ , the Fermi statistics will have a profound influence on  $n(p)$ , whereas the condition  $E_F \ll E_b$  implies that statistical effects are unimportant and  $n(p)$  is well approximated by the classical result. For liquid  $^3\text{He}$  we find  $E_b/E_F \sim 0.5$ , indicating that exchange plays a substantial but not overwhelming role in this system.

As we shall see, experimental determination of  $n(p)$  involves inelastic scattering processes at energy and momentum transfers much larger than the characteristic energy and inverse length scales of the systems under study. In neutron scattering from atomic systems, momentum transfers  $Q$  up to  $\sim 30 \text{\AA}^{-1}$  and energy transfers  $\omega$  up to a few eV are currently attainable. Since these values are much larger than the Fermi energy  $E_F$  and Fermi momentum  $k_F$  for bulk atomic  $^3\text{He}$  (see Table I), a measurement of the momentum distribution of this system would appear to be experimentally feasible.

We turn next to electronic systems. The unit of length conventionally adopted is the Bohr radius  $a_0 = 0.5292 \text{\AA}$ , also called the atomic unit (au). The radius  $r_s$  of the volume per particle, measured in au, lies in the range 2-6 for the conduction-electron subsystem in metals. Hence the characteristic length scale is comparable to that of systems of atoms like liquid helium. However, typical cohesive energies of metals, per atom, run to some tenths of Rydbergs (the conventional unit of energy,  $R = 13.61 \text{ eV}$ ), so the characteristic energy scale is three orders of magnitude larger than in the atomic case. Values for the Fermi energy and momentum associated with the conduction electrons in sodium are quoted in Table I. Comparing the binding and Fermi energies of this system we find  $E_b/E_F \sim 0.3$ . Thus, we expect statistics to have an effect on  $n(p)$  comparable to that in liquid  $^3\text{He}$ , though somewhat larger.

Experimentally, X-ray Compton scattering is used to study the dynamic structure of electronic systems. Typical momentum and energy transfers employed in current work are indicated in Table I. Just as in neutron scattering from a system of  $^3\text{He}$  atoms, these can be much larger than the relevant Fermi momentum and energy. Thus we again infer that the momentum distribution is an experimentally accessible quantity.

Nuclear matter has characteristic length and energy scales which are vastly dif

length is the fermi, which is five orders of magnitude smaller than the Å scale of the atomic and electronic systems. The standard unit of energy is the MeV, which is nine orders of magnitude larger than for the atomic case. In infinite nuclear matter the binding energy per particle,  $E_b$ , is 16 MeV. The characteristic Fermi energies and momenta of nuclear systems, entered in Table I, also differ from those of the atomic and electronic cases by many orders of magnitude. Nevertheless, when we form the dimensionless measure  $E_b/E_F$ , we obtain a value 0.4, putting nuclear matter somewhere between atomic and electronic systems in the importance of quantum statistics.

TABLE I  
SCALES

### DEEP INELASTIC NEUTRON SCATTERING

$$1 \text{ Angstrom}(\text{\AA}) = 10^{-8} \text{ cm}$$

$$1 \text{ meV} = 11.6 \text{ K}$$

$$^3\text{He} \quad E_F = 5.0 \text{ K} \quad k_F = 0.789 \text{\AA}^{-1}$$

$$E_b/E_F = 0.5$$

$$5 \text{\AA}^{-1} \leq Q \leq 30 \text{\AA}^{-1}$$

$$20 \text{ meV} \leq E_i \leq 5000 \text{ meV}$$

### X-RAY COMPTON SCATTERING

$$1 \text{ atomic unit (au)} = 5.29 \times 10^{-9} \text{ cm}$$

$$E = 13.61 \text{ eV}$$

$$\text{Na} \quad E_F = 3.23 \text{ eV} \quad k_F = .486 \text{ p(au)}$$

$$E_b/E_F = 0.3$$

$$2.5 \text{ p(au)} \leq Q \leq 100 \text{ p(au)}$$

$$10 \text{ KeV} \leq E_i \leq 400 \text{ KeV}$$

### QUASIELASTIC ELECTRON NUCLEUS SCATTERING

$$1 \text{ Fermi (fm)} = 10^{-13} \text{ cm} \quad 1 \text{ GeV/c} = 5.06 \text{ fm}^{-1}$$

$$E_F = 38.4 \text{ MeV} \quad k_F = 1.39 \text{ fm}^{-1}$$

$$E_b/E_F = 0.42$$

$$Q \leq 10 \text{ fm}^{-1} (2 \text{ GeV/c}) \quad \text{sometimes quote } Q_4^2 = Q^2 - \omega^2$$

$$500 \text{ MeV} \leq E_i \leq 4 \text{ GeV}$$

nents of the nuclear wave function. The momentum transfers relevant to studies in the energy region of the quasielastic peak, prior to the onset of inelastic processes corresponding to the excitation of internal degrees of freedom of the nucleonic constituents, reach only to  $10 \text{ fm}^{-1}$ . This is just an order of magnitude larger than the characteristic  $k_F$  for nuclear systems. While the excess is not as large, in a relative sense, as in the other two cases, important aspects of the momentum distribution will be experimentally accessible here as well.

*In summary:* The similarities between atomic, electronic, and nuclear systems are striking. Their characteristic energy and length scales may differ by many orders of magnitude; yet they display a comparable balance of binding and exchange effects. They are also similar in the sense that it is feasible to perform scattering measurements for which the momentum and energy transfers are substantially larger than characteristic values of particle momentum and energy in the ground state. With some qualifications to be noted later, such experiments may be considered to measure the pertinent momentum distributions.

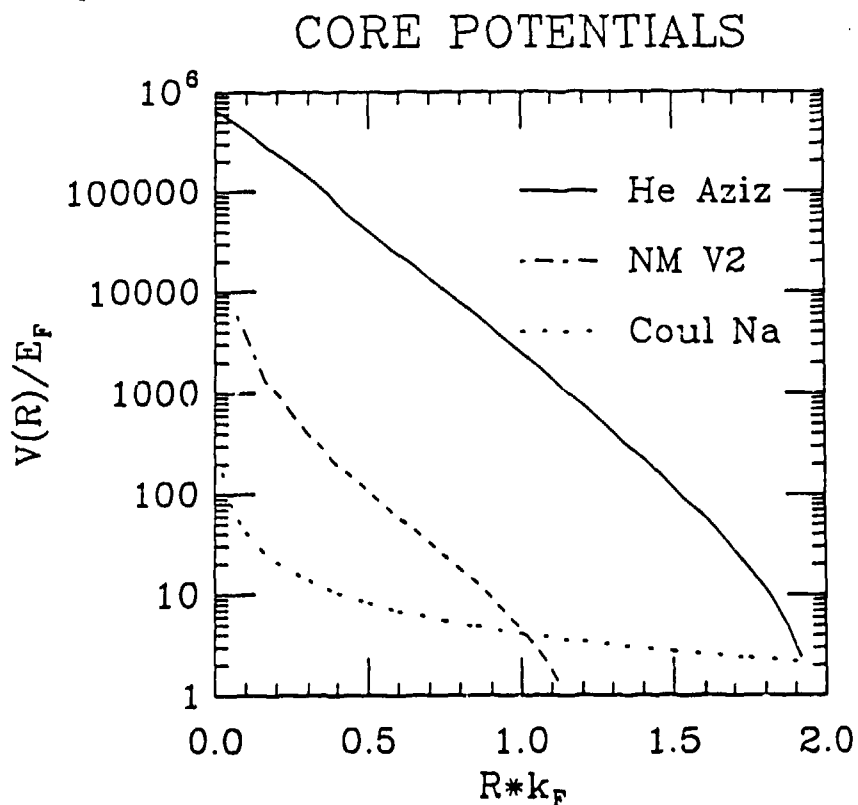


Fig. 3 Typical interaction potential for atomic, electronic, and nuclear, systems. The interaction strength has been scaled by the appropriate Fermi energy and the distance has been scaled by the inverse of the Fermi momentum.

To compare the three systems in another way, we may look at the basic interactions between the atomic, electronic, or nucleonic particles. As expected, these interactions generally differ by many orders of magnitude in their strengths and ranges. To make a sensible comparison, we need to scale the potentials with suitable energy and length measures for the different systems. For the energy measure, we may adopt the Fermi energy, and for the length measure, the inverse of the Fermi momentum is chosen. (Again, comparisons are to be made for a given type of statistics, hence the Fermi case.) Fig. 3 juxtaposes representative potentials for atomic (helium), nuclear, and electronic systems, scaled in this manner. Even when scaled, the potentials differ by orders of magnitude. The helium potential is the strongest at short distances, its core repulsion being very hard (but not infinite). The core of the nuclear potential is two orders of magnitude softer and the electronic (coulombic) potential is two orders of magnitude weaker still.

... are not visible on the semi-log plot. The electronic potential, with a simple monotonic  $1/r$  repulsive behavior, is quite different: while its core is very weak in comparison with the helium and nuclear examples, this potential falls off very slowly at larger  $r$ . As we look at larger distances the electronic potential becomes stronger than the nuclear potential and ultimately surpasses the atomic potential. These differences in the behavior of the basic two-body interactions have interesting consequences for the respective many-body systems. Whereas the strong-coupling limit is at high density in the helium and nuclear problems, it is at low density in the electronic case.

Thus, while there are important similarities between the three classes of systems, there are important differences as well.

## CALCULATION METHODS

Many theoretical methods have been developed to study the momentum distribution of many-body systems. These may be divided into non-stochastic and stochastic approaches. By the former we mean the more traditional, analytically based procedures (like perturbation theory and hypernetted-chain methods) which typically involve manipulations with field-theoretic operators or wave functions and make heavy use of diagrams, before numerical work begins. By the latter, we mean computationally-intensive procedures (like variational, Green's function, and path-integral Monte Carlo methods) based on random-walk algorithms for evaluation of expectation values or thermal averages, or for solution of the Schrödinger equation. The various methods may be further classified according to their ability to handle systems with stronger interparticle couplings. At this point we shall make some general remarks on the strengths and limitations of the most prominent approaches. A more detailed review by Clark and Ristig,<sup>6</sup> including a rather complete set of references, appears later in this volume.

### *Non-Stochastic Methods*

The most familiar examples of non-stochastic methods are ordinary perturbation theory in the bare interaction, starting from the noninteracting system, and variational methods based on independent-particle trial wave functions. Neither approach is useful for predicting the momentum distribution for the systems under study here, either because of the strength of the repulsive core (atomic and nuclear cases) or because of the long range of the interaction (electronic case). On the one hand, rearrangements or resummations of perturbation theory are necessary, and on the other, a viable variational treatment must incorporate dynamical correlations among the particles.

Electronic problems (particularly those involving a uniform electron gas) can often be successfully attacked with perturbation theory, *provided* the ring diagrams are summed to produce a screening of the long-range Coulomb force. This approach is usually framed in terms of Green's functions. The random-phase approximation (RPA), or some variant of it, is used to sum the ring or bubble diagrams in the perturbation expansion of the one-particle Green's function.

Another non-stochastic approach to weakly-interacting electronic systems is band-structure theory, which derives self-consistent one-electron wave functions using a variety of methods including the local-density approximation. This is an eminently practical and highly-developed method for treating the electronic structure of real solids where the lattice plays an essential role, and its successes within Compton-scattering and positron-annihilation studies of momentum distributions have been extensively reviewed elsewhere.<sup>1,7</sup> The limitations of band-structure theory become apparent in dealing with strongly-correlated electronic systems,<sup>8</sup> and our overview of calculational methods will focus on general approaches to strongly-correlated systems.

When applying perturbation-based theories, the main worry is convergence—does the expansion converge, and if so, how fast? For example, perturbative approaches which re-sum only ring diagrams deteriorate or fail as the short-range core of the interaction becomes stronger. They begin to deteriorate for strongly-coupled electronic systems, as represented, say, by the Hubbard model. They fail completely for nuclear and helium systems due to their strongly repulsive cores.

Perturbative techniques can, however, be extended to more strongly interacting systems. Historically, this was first done by Brueckner,<sup>9</sup> his ideas being systematized in terms of a Goldstone diagrammatic expansion.<sup>10,11</sup> When strong repulsive cores are present, it becomes imperative (as a minimum) to re-sum the particle-particle ladder diagrams. This leads to “hole-line expansions” for the quantities of interest, which have seen extensive use in nuclear-matter theory at not-too-high densities. However, the ladder and self-energy resummations which define Brueckner theory do not suffice for very strongly correlated systems like the helium liquids.

In a few cases, analysis to all orders within perturbation theory can be carried out to yield valuable *exact* results, even for very strong couplings. These results typically involve limiting conditions on one or more of the relevant variables, including density, distance, wave number, and temperature. One such result is the prediction of a  $1/p$  singularity in the ground-state  $n(p)$  of a Bose system<sup>3</sup> like liquid  $^4\text{He}$ . Another is the prediction of a Fermi-surface discontinuity in the momentum distribution of all normal Fermi fluids.<sup>12,13</sup>

Self-consistent summation of rings and ladders, leading ultimately to parquet theory<sup>14</sup> offers hope for a comprehensive and quantitative microscopic theory of strongly-coupled systems within the perturbative framework. Unfortunately, this approach has proven exceedingly difficult to implement, especially for Fermi systems. In the interim, variational methods have come to the fore as the most practical means for evaluating the properties of the helium liquids and of nuclear matter at high density.

In the variational approach, a ground state-wave function is chosen on the basis of an intuitive understanding of the correlation structure of the many-body system. The energy expectation value is then minimized with respect to variational parameters or functions appearing in the trial state. The most common trial wave function is the Jastrow form, originally motivated by the requirement that short-range two-body correlations be included in the wave function. It is remarkable that this choice also provides for a correct description of the long-range correlations corresponding to virtual phonons. Although the Jastrow form leads to useful results for the systems under study, the predictions for properties like the ground-state energy and momentum distribution are generally only semi-quantitative.

More sophisticated wave functions, incorporating further aspects of the correlation structure (triplets, momentum-dependent backflow, spin-dependent correlations, noncentral correlations ...) are now in wide use. Quantitative results are obtained for the ground states of liquid  $^4\text{He}$  and  $^3\text{He}$ , and presumably also for the ground states of nuclear and neutron matter. Correlated variational methods have not reached the same state of refinement or popularity in application to the electron gas and other electronic systems. However, they have been rather successful in this context even at the simple Jastrow level (uniform 3D electron gas), or at the (simpler still) Gutzwiller level. Their most dramatic “electronic” success story is found in Laughlin’s theory of the fractional quantum Hall effect.<sup>15</sup>

As described, the variational approach is limited to the ground state. However, variational ideas have been extended to excitations in the correlated random-phase approximation,<sup>16,17</sup> derived from the Dirac-Frenkel time-dependent variational principle. Moreover, the variational approach has been extended to the evaluation of equilibrium properties of quantum fluids at finite, but low, temperatures.<sup>18</sup>

In variational approaches to atomic, nuclear, and electronic systems, the counterpart of the convergence worry of perturbation theory is the problem of reliable

calculation of expectation values and matrix elements with respect to correlated wave functions. This highly nontrivial problem is discussed by Clark and Ristig<sup>6</sup> and will not be considered here in any detail. Depending on the application and the sophistication of the wave functions, higher-order cluster diagrams contributing to correlated expressions may be either partially re-summed, approximated, or ignored. Current practice<sup>19,20</sup> involves the use of "scaling procedures" to simulate the effects of higher-order terms which are difficult or impossible to evaluate explicitly.

A deeper problem of more conceptual weight is the constraint which the choice of wave function imposes on the physical description. Lacking the right intuition, the proposed wave function will not have sufficient freedom, and interesting phenomena (for example, phase transitions) may be missed. There exist stability tests which make this drawback less serious, but these tests usually refer only to local stability. Recent work with shadow wave functions<sup>21</sup> introduces a welcome flexibility which reduces the reliance on intuition.

A related criticism of the variational approach is that improvements are not very systematic. This criticism may be answered by an extension of variational theory known as the method of correlated basis functions<sup>22,23</sup> (CBF). In CBF a basis of functions is generated by applying a correlation operator determined variationally, to a complete set of model wave functions suitable for a weakly interacting system (e.g. Slater determinants). This scheme combines the insights and techniques of the variational approach to strong interactions, with the formal advantages of perturbation theory and other approaches (e.g. RPA, BCS, etc.) designed for weak interactions. Of course, the method will also suffer (in lesser degrees) from the same kind of convergence worries which plague these underlying approaches. Although complicated in appearance, CBF is one of the more efficient, quantitative, and powerful of the non-stochastic approaches, yielding a variety of useful results for atomic, nuclear, and electronic systems.

### *Stochastic Methods*

The available non-stochastic techniques all experience some degree of difficulty in handling very strong interactions. Such a difficulty is not intrinsic to the stochastic approaches, although some "hangover" may be experienced since the implementation of stochastic treatments usually relies on information provided by a prior non-stochastic study. Another (related) advantage is that stochastic methods are immune to the convergence problems which beset perturbative and variational procedures. On the negative side of the ledger, stochastic methods suffer from the well-known disadvantages of computer-intensive, "granular" simulations.

The variational Monte Carlo (VMC) method contains basically the same physics as the variational approach described under non-stochastic methods. However, a Metropolis Monte Carlo algorithm is used to evaluate the many-body integrals. This technique is superior to those employed in non-stochastic variational theory, such as hypernetted-chain re-summation, since higher-order cluster diagrams are automatically included. The statistical errors associated with the Metropolis algorithm can be effectively controlled by variance reduction techniques. Perhaps the major concern is that (for obvious practical reasons) the simulations are performed for a sample of a few dozen or a few hundred particles, instead of extended medium. Periodic boundary conditions are imposed in a finite cube, with side length adjusted to give the pre-assigned average particle density. Finite-box-size effects can be significant, especially for the long-range behavior of the one-body density matrix, though they are generally believed to be of little importance.

Needless to say, VMC suffers from the same intrinsic limitations as its non-stochastic counterpart. Unless the general nature of the interesting physics is known in advance, the variational approach may pass it by.

A more powerful alternative is the Green's function Monte Carlo (GFMC)

From the Schrödinger equation, in imaginary time, may be mapped into a diffusion equation in real time, which may in turn be solved by Monte Carlo techniques. In principle, this approach leads to the exact ground state. In practice, it works exceedingly well in application to Bose systems, such as liquid  $^4\text{He}$ , where the ground-state wave function is positive. As usual, there are statistical errors (arising in the solution of the Schrödinger equation as well as in the evaluation of various quantities), but again these can be controlled by various techniques. There are also finite-box-size effects, since again one must work with a finite number of atoms. In particular, the size of the simulation box limits the accuracy of GFMC predictions of the large- $r$  behavior of the exact  $\rho_1(r)$  and consequently the singular behavior of  $n(p)$  at small  $p$  is missed. Otherwise, state-of-the-art predictions for the momentum distribution and the condensate fraction are obtained.<sup>24</sup>

While the treatment of Bose systems in GFMC is relatively easy, Fermi applications remain problematic. The antisymmetry requirement, a global property, is hard to build into the diffusion algorithm, which is by nature local. In straightforward application, the fact that the wave function is not of one sign leads to an exponential growth of the statistical error. Nevertheless, approximate realizations of GFMC—e.g. the fixed-node approximation and transient estimation—may be used to obtain quantitatively reliable results<sup>24,25</sup> for liquid  $^3\text{He}$ . Even so, much work remains to be done to bring the fermion problem to an aesthetically satisfactory conclusion.

Apart from this specific Fermi difficulty, the GFMC treatment should eventually converge to the exact ground-state wave function of the fermion or boson system. However, in practice, with finite running time, this may not be the case. Importance sampling is used to speed the convergence of the calculation, but it may also prejudice the final results. An initial trial wave function, taken say from non-stochastic variational theory, is commonly used as an importance function to select the most likely configurations. If this wave function is not close to the true ground-state wave function, but represents instead some sort of metastable state, the method may not get the chance to find totally new or unexpected features of the many-body system.

Recently, in a beautiful implementation of Richard Feynman's view of quantum theory, Ceperley<sup>26</sup> has developed path-integral Monte Carlo (PIMC) methods to evaluate the equilibrium properties of quantum fluids at finite temperatures. The calculation begins with an accurate representation of the density matrix at high temperatures. A lower-temperature density matrix is then constructed from a path integral over products of high-temperature density matrices. Metropolis-type algorithms allow accurate results to be obtained for the properties of liquid  $^4\text{He}$  over a broad range of temperatures and pressures.

## IMPULSE APPROXIMATION

In previous sections we have compared and contrasted the theoretical issues which are important to momentum distribution studies in different systems. As we scan from atomic systems through electronic and nuclear systems all the way to particle physics, we have covered ten orders of magnitude range in energies, momenta, and interaction strengths. Nevertheless, we have found many common conceptual elements and calculational approaches. In the present section, we show that experimental studies of momentum distributions also share common themes across this extraordinary dynamic range. Momentum distributions are usually measured by scattering experiments in which the energy and momentum transferred are very high compared to the energies and momenta characteristic of ground-state properties and collective behavior. In this limit, the scattering law may be related to the momentum distribution by invoking the *impulse approximation*, which assumes that a single particle of the system is struck by the scattering probe, and that this particle recoils freely from the collision.

Such experiments began with the discovery of the Compton effect<sup>27</sup> in the scattering of X-rays from electrons in metals.<sup>28</sup> Today, neutron scattering at energies of

energies of tens of keV is used to measure  $n(p)$  in electronic systems, and electron scattering at GeV energies is used to measure  $n(p)$  in nuclei and inside nucleons. In all cases, the observation of appropriate scaling<sup>29</sup> (e.g. "Y-scaling") behavior of the cross section is presumed to indicate that conditions for the validity of the impulse approximation have been approached. Violations of this scaling are also of interest. They can arise from excitation of internal degrees of freedom ("scale breaking"), or they can be due to breakdowns of the impulse approximation such as final-state interactions of the struck particle, etc. In all cases, the measured quantity is a "Compton profile," with amounts to a projection of the momentum distribution onto one dimension. The various experimental settings entail common data analysis and methodological questions. In this section we shall elaborate on these common elements of the measurement of momentum distributions.

### *Deep-Inelastic Neutron Scattering*

The scattering of neutrons by an atomic system is described by the double differential scattering cross section, which is the scattering per unit solid angle and per unit energy. This is calculated in first Born approximation, the interaction of a neutron with an atom being expressed as a Fermi pseudopotential proportional to the scattering length. In neutron scattering the cross section is traditionally written as<sup>30</sup>

$$\frac{d^2\sigma}{d\omega d\Omega} = \frac{\sigma_T}{4\pi} \frac{k_i}{k_f} S(Q, \omega) , \quad (5.1)$$

where  $\sigma_T$  is the total scattering cross section for a single atom and  $k_i$  and  $k_f$  are the initial and final neutron wave vectors. The interaction of the neutron with the sample is described by the dynamic structure factor  $S(Q, \omega)$ , with energy transfer  $\omega = (\hbar^2/2m_n)(k_i^2 - k_f^2)$  and momentum transfer  $Q = |k_i - k_f|$ .

The dynamic structure factor is the Fourier frequency transform of the density-density correlation function of the sample. It is convenient to separate the structure function into two components

$$S(Q, \omega) = \frac{\sigma_{coh}}{\sigma_T} S_{coh}(Q, \omega) + \frac{\sigma_{coh} + \sigma_{inc}}{\sigma_T} S_{inc}(Q, \omega) . \quad (5.2)$$

In the first term,  $S_{coh}$  is the coherent structure factor<sup>31</sup> and represents density fluctuations which involve *different* atoms. Thus

$$S_{coh}(Q, \omega) = \frac{1}{\pi N} \text{Re} \int_0^\infty dt e^{i\omega t} \sum_{i \neq j} \langle \Psi_0 | e^{-i\vec{Q} \cdot \vec{r}_i(t)} e^{i\vec{Q} \cdot \vec{r}_j(0)} | \Psi_0 \rangle , \quad (5.3)$$

where  $\vec{r}_i(t)$  and  $\vec{r}_j(t)$  are the time dependent positions of the two atoms, and  $\Psi_0$  is the wave function for the initial state of the system before the scattering. This term describes the collective behavior of many atoms including collective excitations, crystalline order, etc. The second term  $S_{inc}$  is the incoherent structure factor, which only involves the motion of single atoms. Again, this may be written as the Fourier transform of a time correlation function

$$S_{inc}(Q, \omega) = \frac{1}{\pi N} \text{Re} \int_0^\infty dt e^{i\omega t} \sum_i \langle \Psi_0 | e^{-i\vec{Q} \cdot \vec{r}_i(t)} e^{i\vec{Q} \cdot \vec{r}_i(0)} | \Psi_0 \rangle , \quad (5.4)$$

which now only involves the scattering from a single atom at different times. Consequently, this structure factor will be sensitive to single-particle motions such as self diffusion and, as we will see, the momentum distribution.



to the interatomic spacing. For  $Q$  in excess of these momenta, the exponentials in (5.3) will then oscillate rapidly from atom to atom and, on average, cancel out. Therefore,  $S_{coh}$  will not contribute in the high- $Q$  limit and only  $S_{inc}$  will be left. This is the limit of importance to momentum distribution experiments, so we may focus on the scattering from individual atoms, commonly referred to as "Deep-Inelastic Neutron Scattering."<sup>32</sup>

If, in addition, the energy transferred to an atom by a neutron is large compared with the potential energies due to neighboring atoms, the final state of the struck atom will then be that of a free particle. Under these conditions, the incoherent scattering function reduces to the well-known "Impulse Approximation"<sup>33</sup> (IA), so called because the scattering particle is supposed to impart a momentum to the struck atom in a time so short that neighboring atoms are unable to respond. Then

$$S_{IA}(Q, \omega) = \frac{1}{\rho} \int \frac{d\vec{p}}{(2\pi)^3} n(|\vec{p}|) \delta\left(\omega - \frac{Q^2}{2M} + \frac{\vec{Q} \cdot \vec{p}}{M}\right), \quad (5.5)$$

where  $M$  is the mass of the struck atom.

The scattering law (5.5) exhibits characteristic features which have often been used as an indication that conditions for the validity of the IA have been reached. The scattering is centered at and symmetric about the recoil energy  $\omega_r = Q^2/2M$ . In neutron scattering the location of the scattering peak is determined by the mass of the struck particle and different constituents in the sample can be separated by their different recoil energies. In addition, the width of the observed scattering, at constant  $Q$ , is proportional to  $Q$  times the width of the momentum distribution. In the IA limit, the scattering is no longer a function of the energy and momentum transfer separately. For isotropic systems, where  $n(p)$  depends only on the magnitude of  $p$ , the scattering becomes a function of a single variable

$$Y = \frac{M}{Q} \left( \omega - \frac{Q^2}{2M} \right), \quad (5.6)$$

which is just the longitudinal momentum,  $p_{||}$ . The scattering law may then be rewritten

$$J_{IA}(Y) = \frac{Q}{M} S_{IA}(Q, \omega) = \frac{1}{4\pi^2 \rho} \int_{|Y|}^{\infty} dp p n(p). \quad (5.7)$$

The function  $J_{IA}(Y)$  is known as the Compton profile. The asymptotic behavior expressed by (5.7), called  $Y$  scaling, was first emphasized by West<sup>34</sup> in the context of electron scattering from nuclei. It is of course more broadly applicable to scattering processes that meet the criteria for application of the impulse approximation. On the other hand, we must point out that  $Y$ -scaling is a necessary but not a sufficient condition for validity of the impulse approximation. For example, in systems with hard-core potentials,  $Y$ -scaling is predicted at high  $Q$  even though the impulse approximation does not hold.<sup>35,36</sup>

As an illustration of this kind of scaling, consider the scattering from liquid helium,<sup>37</sup> plotted in Fig. 4 as  $J(Y)$ , at  $Q$ 's of 7, 12, and 23  $\text{\AA}^{-1}$ . When the experimental data for  $S(Q, \omega)$  is plotted versus  $\omega$  (not shown), the peak centers and widths vary greatly with  $Q$ . However, when converted to  $J(Y)$  these results nicely demonstrate the predicted  $Y$ -scaling behavior. The scattering is symmetric and centered at  $Y=0$ , and the width of the scattering is independent of the momentum transfer  $Q$  of the measurement.

While Fig. 4 illustrates the expected  $Y$ -scaling behavior, deviations are in fact evident. The measurements at the highest  $Q$  (23  $\text{\AA}^{-1}$ ) agree best with the impulse-approximation predictions. At the lower  $Q$ 's one sees significant deviations from IA

and other deviations from the predictions of the impulse approximation are of great importance in experimental determinations of the momentum distribution in real experiments where  $Q$ , while large, is still finite. Such discrepancies have been termed "Final-State Effects," because they are thought to arise from the interactions of the struck atom with neighboring atoms. Another factor may be the binding of the target atom in the condensed phase, an 'initial state effect' which is ignored in deriving the impulse approximation. Deviations from the IA have received considerable theoretical attention and will be discussed more fully later.

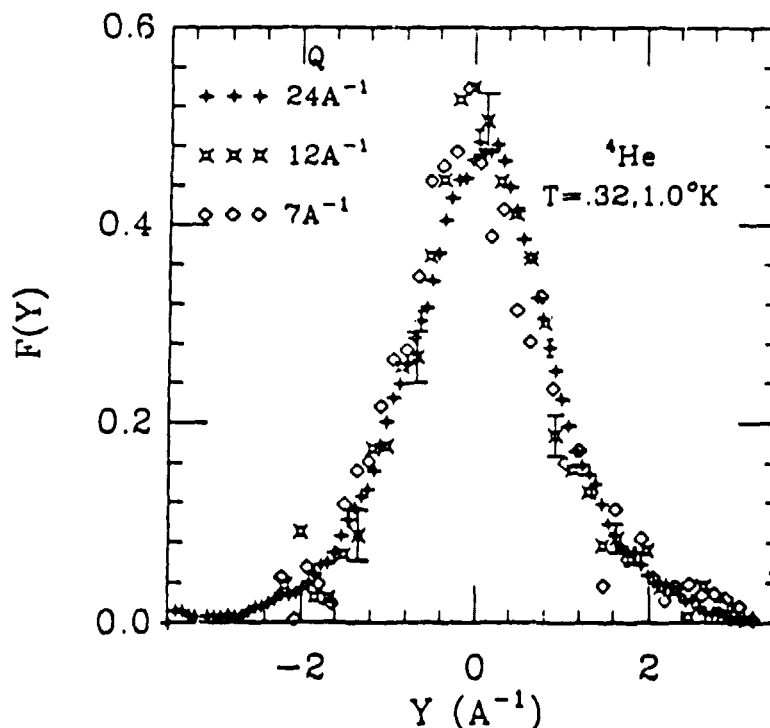


Fig. 4 Inelastic neutron scattering from liquid  ${}^4\text{He}$  at momentum transfers of  $7 \text{ \AA}^{-1}$ ,  $12 \text{ \AA}^{-1}$  (at  $1.0 \text{ K}$ ) and  $24 \text{ \AA}^{-1}$  (at  $0.35 \text{ K}$ ). The results, plotted as  $J(Y)$ , all fall on approximately the same curve illustrating the  $Y$ -scaling behavior (from ref 37).

### Compton Scattering

An appropriate probe of electronic systems is the photon, whose coupling to the electron charge is also well described in first-order perturbation theory. The theoretical discussion proceeds in close analogy with that for neutron scattering from atoms. Accordingly, when the momentum transferred by the photon is large compared to the interelectronic spacing, the properties of individual electrons are probed. This condition, corresponding to what is termed Compton scattering, is met for photons at hard X-ray energies (tens of KeV). Compton scattering is the basis of the earliest of the momentum distribution experiments.<sup>38</sup> It has yielded considerable information on the electronic structure of systems in condensed phases.<sup>1</sup>

The cross section for the scattering of photons by a system of electrons in the high- $Q$  regime is

$$\frac{d^2\sigma}{d\Omega d\omega} = \left( \frac{d\sigma}{d\Omega} \right)_0 \frac{\omega_2}{\omega_1} \frac{m_e}{Q} \int d\vec{p} n(|\vec{p}|) \delta \left( \omega - \frac{Q^2}{2m_e} + \frac{\vec{Q} \cdot \vec{p}}{m_e} \right), \quad (5.8)$$

where  $\omega_1$  and  $\omega_2$  are the frequencies of the incident and scattered photon,  $Q$  is the momentum transferred by the photon, and  $m_e$  is the mass of the electron. The

section. As in the impulse approximation to the neutron-scattering problem, the double-differential cross section in the Compton-scattering case may be expressed in terms of a single scaling variable,  $Y$ . It is given by some trivial factors, times the Compton profile

$$J(Y) = \int_{p_x} \int_{p_y} n(p_x, p_y, Y) dp_x dp_y \quad (5.9)$$

Here, we have written the Compton profile in a form which highlights its interpretation as the longitudinal momentum distribution, obtained by integrating  $n(p)$  over the components of  $p$  transverse to  $Q$ .

The cross section for Compton scattering consists of a spin-independent and a spin-dependent component. The spin-independent component, which corresponds to the dominant mechanism for the scattering of unpolarized X-rays, is associated with the elementary Thompson cross section

$$\left. \frac{d\sigma}{d\Omega} \right|_0 = \left( \frac{e^2}{m_e c^2} \right)^2 \quad (5.10)$$

where  $e$  is the charge of the electron and  $c$  is the speed of light. In measuring this component of the scattering, one probes the full electronic  $n(p)$ , irrespective of the spin of the electron.

The spin-dependent component

$$\left. \frac{d\sigma_s}{d\Omega} \right|_0 = \left( \frac{e^2}{m_e c^2} \right)^2 \left( \frac{\omega_2}{\omega_1} \right)^2 \left( \frac{1 - \cos(\phi)}{m_e c} \right) \vec{S} \cdot (\vec{k}_1 \cos(\phi) - \vec{k}_2) \quad (5.11)$$

where  $\vec{k}_1$  and  $\vec{k}_2$  are the incident and final wavevector of the photon,  $\phi$  is the scattering angle, and  $\vec{S}$  is the spin of the electron. This component is only of interest for polarized radiation. Using polarized X-rays, the momentum distribution of one particular spin state can be measured. With the recent developments in synchrotron radiation sources, magnetic Compton scattering studies of the spin-dependent momentum distribution have become practical.

In Compton scattering, the struck particle is always an electron and the scattering peak is always centered at  $Q^2/2m_e$ . However, the structure of the scattering peak may be used to separate the contributions from different 'types of electrons,' such as conduction and core electrons. The width of a Compton profile is proportional to  $Q\Delta p/m_e$ , where  $\Delta p$  is the width of the momentum distribution. The core electrons, which are tightly bound, will have a broad profile, while the conduction electrons, which are in extended plane-wave states, will have a relatively narrow profile. Fig. 5 illustrates this distinction using the Compton profile of beryllium. The narrow contribution results from the conduction electrons, while the broad background is due to the tightly bound core electrons. The sharp change in slope of the scattering, which is due to the jump in  $n(p)$  at the Fermi surface of the conduction electrons, is also clearly visible.

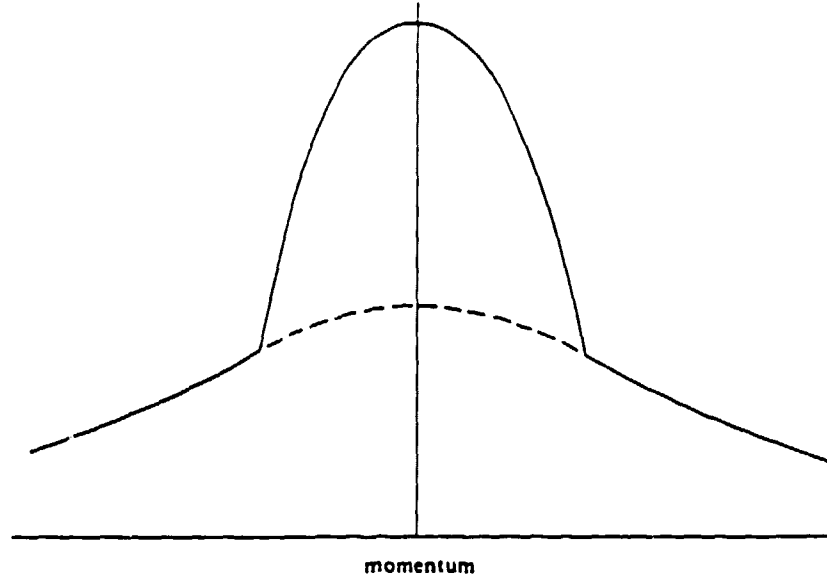


Fig. 5 Schematic illustration of the Compton profile from beryllium. The broad component, which has been extended through the central region by the dashed line, is due to the tightly bound core electrons. The narrow component is due to the nearly free conduction electrons. The sharp change in slope at the Fermi surface is clearly visible (from ref 28).

### *Quasielastic Electron-Nucleus Scattering*

The appropriate probe for studying the momentum distribution of nucleons in nuclei is the electron, which couples electromagnetically to nucleons. The situation here is much more complicated than in electronic and atomic systems. It is important to use relativistic kinematics in describing the scattering. Moreover, the nucleon-nucleon interaction is incompletely characterized, and its complexity makes theoretical calculations difficult. Most important, internal degrees of freedom of the nucleons are easy to excite with the energy and momentum transfers required to approach conditions for validity of the impulse approximation.

The impulse-approximation result for the scattering of electrons by the nucleus is

$$S_{IA}(Q, \omega) = \frac{\nu}{\rho} \int_M^\infty \frac{d\sigma(Q)}{dM_E} \int \frac{d\vec{p}}{(2\pi)^3} n(|\vec{p}|) \delta(\omega - \sqrt{M_E^2 + (Q + p)^2} + \sqrt{M^2 + p^2}) \quad (5.12)$$

where  $\nu$  is the single-particle level degeneracy ( $=4$ ),  $n(p)$  is the momentum distribution of nucleons in the ground state of the target, and  $d\sigma(Q)/dM_E$  is the cross section for electron scattering from a single nucleon leading to an excitation of the nucleon with rest mass  $M_E$  (e.g. excitation of the  $\Delta(1238 \text{ MeV})$ ).

Y-scaling is predicted by the impulse approximation only if subnucleonic degrees of freedom are not excited, and the final mass of the recoiling constituent(s) ( $M_E$ )

as "quasielastic electron-nucleus scattering" (QENS), places upper bounds on the applicable momentum and energy transfers. The associated scaling function is given by

$$F_{IA}(Y) = \frac{QS_{IA}(Q, \omega)}{(\omega + M)} \sigma_{el}(Q) = \frac{\nu}{4\pi^2 \rho} \int_{|Y|}^{\infty} dp \, pn(p) \quad , \quad (5.13)$$

which is similar to the formulae arising in deep-inelastic neutron scattering and Compton scattering. With relativistic kinematics, the scaling variable  $Y$  now takes the somewhat different form

$$Y = p_{||} = \frac{M}{Q} \left( \omega - \frac{Q^2}{2M} + \frac{\omega^2}{2M} \right) \quad . \quad (5.14)$$

Because in QENS the energy and momentum transfers are limited by the necessity to avoid the excitation of nucleonic internal degrees of freedom, it is difficult to achieve momentum transfers more than a few times larger than the characteristic momenta of nucleons in a nucleus, and  $Y$ -scaling is observed only for negative  $Y$ . This  $Y$ -scaling portion of the cross section corresponds to the high- $p$  components in the tail of the momentum distribution. Of course, it is just these high- $p$  components which provide the most information on short-range correlations in nuclei.

Another consequence of the limited ranges of energy and momentum transfers in QENS is that the off-shell character of the target particle in the many-body medium, prior to collision with the probe, can be far more important than in neutron or Compton scattering. Thus, while scaling behavior may still be observed, one needs to modify the scaling variable to take account of the binding of the constituent particles. In particular, Sick and coworkers<sup>39,40</sup> proposed using  $Y_S = p_{||}$  as determined from the kinematic relation

$$[(p + Q)^2 + M^2]^{1/2} - M = \omega - SE \quad , \quad (5.15)$$

where the constant shift  $SE$  is a suitable average separation energy for removal of a nucleon from the nucleus, and irrelevant recoil effects have been omitted. Improved scaling plots of data are obtained in terms of  $Y_S$ . Other forms for the scaling variable have been proposed as well, notably in attempts to incorporate effects of "final-state interactions" into the analysis.<sup>41</sup>

As an example of quasielastic electron-nucleus scattering, analyzed in terms of the variable  $Y_S$ , consider the results for a carbon target<sup>40</sup> shown in Fig. 6. For  $Y_S$  below  $-0.1$ , the experimental results nicely illustrate the  $Y$ -scaling predictions. Around  $Y_S = 0$  and above, the breakdown of  $Y$  scaling is seen as internal degrees of freedom of the nucleon are excited.

The behavior illustrated in Fig. 6 is all the more impressive when one notes that the scattering intensity changes by almost four orders of magnitude over the kinematic range in  $Y_S$  for which scaling appears to hold. In contrast, the  $Y$ -scaling plot for  $^4\text{He}$  shown in Fig. 4 extends over less than two orders of magnitude in the scattering intensity. This disparity is due to the much higher backgrounds which prevail in current neutron-scattering experiments, as compared with QENS. In the nuclear work, the results found in the regime of large  $-Y_S$  are suggestive of an exponential fall-off of the momentum distribution which might be a general feature of strongly-interacting many-body systems. It would be of great interest to test this conjecture in future neutron-scattering experiments on quantum fluids.

Before turning to other issues, we would like to address the unfortunate semantic confusion which can arise in trying to compare the three types of experiments: deep-inelastic neutron scattering, Compton scattering, and quasielastic electron-nucleus scattering. In condensed-matter physics, "Quasi-Elastic Neutron Scattering" (also QENS) refers to scattering measurements in which the energy transfer is small, as

refers to any scattering process in which the initial and final energies of the scattering (probe) particle are significantly different. "Deep-Inelastic Neutron Scattering" refers to higher-energy-transfer experiments which are aptly described in terms of scattering off single atoms in condensed-matter systems. In nuclear physics, inelastic scattering refers instead to cases in which there is excitation of nucleonic substructure, including any process which creates new particles. Thus, even though the energy of the scattering electron may change substantially in quasielastic electron-nucleus scattering, the process is termed "quasielastic" because the recoiling constituent particle has the same rest mass as it did before the collision. Finally, "Deep-Inelastic Electron-Nucleus Scattering" refers to experiments which are best described in terms of scattering off the probe electrons off the quark constituents of nucleons.

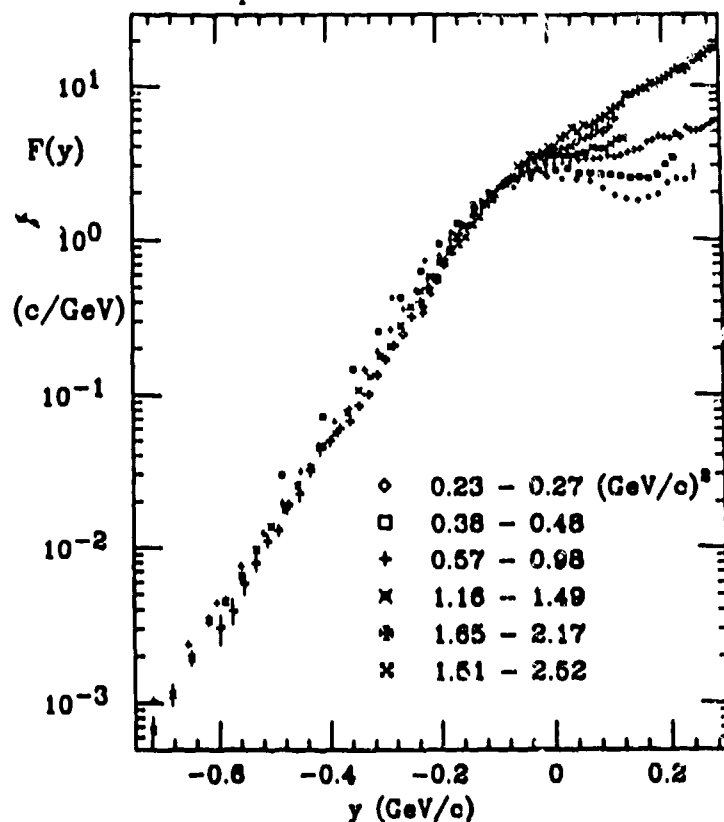


Fig. 6 Quasielastic Electron Nucleon Scattering (QENS) from  $^{13}\text{C}$  at several different momentum transfers. For  $Y > .1 \text{ GeV/c}$  the results all fall on the same curve, illustrating the  $Y$ -scaling behavior.  $Y$ -scaling breaks down for larger values of  $Y$  due to the excitation of internal degrees of freedom of the nucleon (from ref 40).

### Final State Effects

As described above, the measurements of the momentum distribution in atomic, nuclear, and electronic systems by scattering experiments all depend implicitly on the validity of the impulse approximation. The impulse approximation assumes that the particle probe (neutron, photon, electron) scatters off a single particle (atom, electron, nucleon) in the many-body system in a time so short that the particles neighboring the struck particle have no time to react to the perturbation caused by the probe. The response of the struck particle is determined entirely by its initial momentum distribution, and it recoils from the collision in a free-particle state of high momentum and energy. Obviously, this description becomes more accurate the higher the momentum and energy transferred in the scattering process (i.e. the shorter the probe/struck-particle interaction time), and the weaker the interactions between the struck particle and its neighbors.

In real experiments where the momentum and energy transfers are finite and in-

atom-atom interactions; in nuclear problems, from nucleon-nucleon interactions; and in Compton scattering, from both electron-electron and electron-ion core interactions and orthogonalization. The important questions then are the size and form of the deviations from the impulse approximation and the extent to which they limit our ability to infer the single-particle momentum distribution from scattering data.

At high momentum and energy transfers, the most important deviations from the impulse approximation are due to collisions of the recoiling particle with its neighbors, which are called final-state effects. Hohenberg and Platzman<sup>33</sup> considered this problem for deep-inelastic neutron scattering from helium. Elementary arguments lead to the prediction that the impulse-approximation result will experience a Lorentzian broadening with width

$$\Delta Y_{FWHM} \approx \rho \sigma_{tot}(Q) , \quad (5.16)$$

where  $\sigma_{tot}(Q)$  is the atom-atom scattering cross section. Heuristically, in terms of the uncertainty principle, this broadening is due to the finite 'lifetime' of the struck particle before it collides with its neighbors. The simple result (5.16) for the width of final-state broadening holds in several of the modern theories for FSE. However, there is much debate over the details of the lineshape. For one thing, the original Hohenberg-Platzman Lorentzian-broadening model cannot be rigorously correct since it violates the  $\omega^2$  sum rule on  $S(Q, \omega)$ .

Equation (5.16) suffices to indicate the properties which are most important in determining the FSE in real systems. FSE are larger for stronger interactions between particles and lower momentum transfers. Two idealized examples bracket the physical cases: In the noninteracting gas, FSE are entirely lacking, and  $Y$ -scaling holds trivially. At the other extreme of a gas of hard spheres, FSE are always present, even at infinite  $Q$ . Nevertheless, as we have already remarked,  $Y$ -scaling is predicted for the limiting case of hard-core interactions even though the impulse approximation is not valid. The repulsive cores for the real systems of interest to us are plotted in Fig. 3. (The attractive portion of the potential plays a negligible role in FSE.) Real systems may be ranked in *descending* order as follows, according to the strength of the core potential, appropriately scaled in terms of the characteristic momenta: atomic systems such as helium quantum fluids; nucleons in nuclei; electronic systems; and finally color-neutral systems of quarks and gluons. In *ascending* order, the ranking of the corresponding inclusive scattering experiments according to maximal momentum transfers, again scaled with characteristic momenta, is: quasielastic electron-nucleus scattering; deep-inelastic neutron scattering; Compton scattering; and deep-inelastic scattering of electrons from nucleons (which really refers to scattering off their constituent quarks and gluons). Thus, FSE are expected to be significant for both deep-inelastic neutron scattering (DINS) on quantum fluids and quasi-elastic electron-nucleus scattering (QENS), while they are more readily avoided in Compton scattering on electronic systems and are absent in particle physics.

An important consequence of (5.16) for deep-inelastic neutron scattering is that the approach to the impulse approximation will be very slow with increasing  $Q$ , because the  $\sigma_{tot}(Q)$  decreases logarithmically with  $Q$  for He-He scattering. Therefore, helium is very close to a hard-sphere system where approximate  $Y$ -scaling behavior is obtained without the impulse approximation being valid. The final-state broadening interferes with observation of the features in the momentum distribution which are the most interesting, i.e. the Bose condensate peak in  $^4\text{He}$  and the Fermi surface discontinuity in  $^3\text{He}$ . While in QENS the  $\sigma_{tot}(Q)$  falls more rapidly with increasing  $Q$ , the obtainable  $Q$ 's are comparatively much smaller when scaled by characteristic momenta.

Any attempt to determine momentum distributions in DINS and QENS must somehow take into account the final-state effects. At present, we depend on theoretical calculations to provide the appropriate corrections. Unfortunately, this adds another layer of complication and uncertainty to the interpretation of the experimen-

quantitative characterization of FSE presents a major challenge for many-body theorists. Apart from highly nontrivial dynamical considerations, this problem involves aspects of the strongly-interacting ground state (e.g., the two-body reduced density matrix) which are difficult to evaluate. However, if we assume that the many-body calculations of momentum distributions are correct, theories for FSE can be tested using scattering data.<sup>42</sup>

The recent non-Lorentzian broadening theory by Silver<sup>43</sup> for  $^4\text{He}$ , based on earlier work by Gersch and Rodriguez<sup>44</sup> yields the broadening function shown in Fig. 7, which is to be convoluted with the impulse-approximation prediction, Eq. (5.7), to obtain the predicted scattering. While the FWHM of the function in Fig. 7 is comparable to that from the Hohenberg-Platzman Lorentzian-broadening theory, Eq. (5.16), Silver's theory has negative wings at large  $|Y|$  so that it satisfies the  $\omega^2$  sum rule which requires that the second moment of the broadening function be zero. The additional physics which this theory takes into account is the pair-correlation function of the interacting ground state, which governs the collision rate as a function of recoil distance. The overall effect of final-state broadening predicted by Silver is much smaller than in the original Hohenberg-Platzman treatment, and it produces excellent agreement with the recent experiments of Sosnick *et al.* as discussed further in the next section.<sup>45</sup>

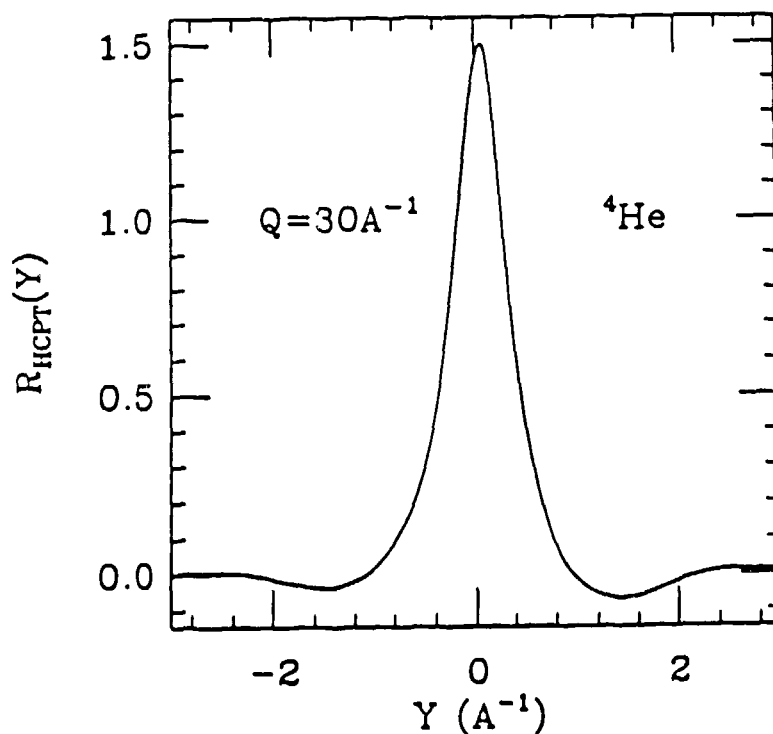


Fig. 7 Final State Effect broadening function  $R(Y)$  for  $^4\text{He}$ . The width of the central peak is approximately  $\rho\sigma(Q)$ , where  $\sigma(Q)$  is the atom-atom scattering cross section, in agreement with simple 'lifetime' arguments. The negative wings are required to satisfy the  $\omega^2$  sum rule (from ref 43).

### Scale Breaking

Deviations from  $Y$ -scaling may arise from final-state interactions, but a more fundamental cause is the excitation of internal degrees of freedom of the constituent particles of the sample. The latter effect is often referred to as "scale breaking." We have already seen that such scale breaking may occur in the nuclear context. It is also present in measurements of momentum distributions in other kinds of systems.



First, consider the scattering of neutrons by a collection of atoms. Fig. 8 shows an overview of the scattering function in the  $Q - \omega$  plane for a simple atom with no internal excitations. At low  $Q$  and  $\omega$  the scattering is due to collective excitations - phonons, rotons, diffusive modes, Bragg scattering, etc. At higher momentum transfers the collective excitations are damped out and the scattering is dominated by single-particle excitations. Finally, at large enough  $Q$ 's, the scattering is described by the IA, and information on  $n(p)$  can be obtained.

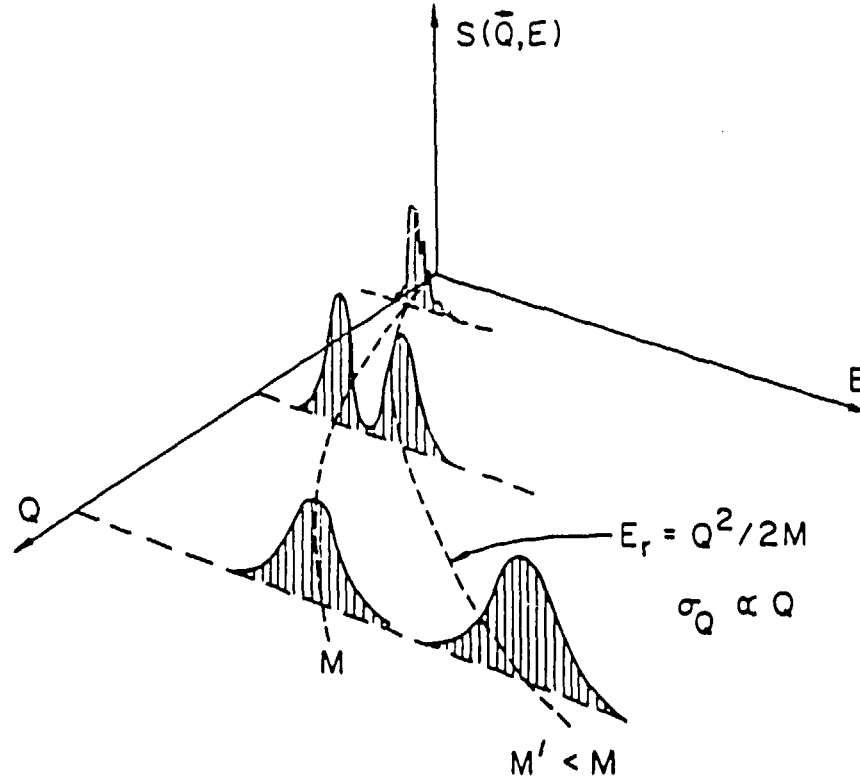


Fig. 8 Schematic of the dynamic structure factor  $S(Q, \omega)$  as a function of energy and momentum transfer. The scattering at low  $Q$  and  $\omega$  is dominated by collective excitations - phonons, rotons, diffusive modes, Bragg scattering, etc. At higher  $Q$  and  $\omega$  the collective excitations are damped and the single particle properties determine the scattering. At very high  $Q$  and  $\omega$  the scattering is described by the IA. In this region the peak is centered at the recoil energy ( $Q^2/2m$ ) and the width of the peak is proportional to  $Q$ . The scattering from particles with two different masses is shown to illustrate the ability to separate the scattering from different constituents of the sample is the IA regime (From ref 46).

Scale breaking can be illustrated by the scattering from a molecule which has both translational and internal degrees of freedom. Bulk molecular hydrogen furnishes an excellent example. The translational and internal modes (the latter consisting of vibrations and rotations of the molecule about its center of mass) are essentially decoupled. The IA is easily generalized to give

$$S_{IA}(Q, \omega) = \sum_n \frac{f_n}{\rho} \int \frac{d\vec{p}}{(2\pi)^3} n(|\vec{p}|) \delta\left(\omega - \omega_n - \frac{Q^2}{2M} + \frac{\vec{Q} \cdot \vec{p}}{M}\right), \quad (5.17)$$

where  $f_n$  and  $\omega_n$  are respectively the structure factor and energy of the  $n^{\text{th}}$  internal excitation. Fig. 9 shows the scattering from hydrogen<sup>47</sup> when two internal excitations, rotational excitations in this case, are excited. The rotational excitations shift

two shifted peaks, which can be resolved in this case.  $Y$ -scaling breaks down when multiple internal excitations are excited. At low energy transfers, only the first rotational excitation is excited and a unique scaling variable can be defined. However, at higher energy transfers many different excitations contribute to the scattering, each centered at a different energy. It is clear that no unique scaling variable can be defined in this case and that  $Y$ -scaling will break down.

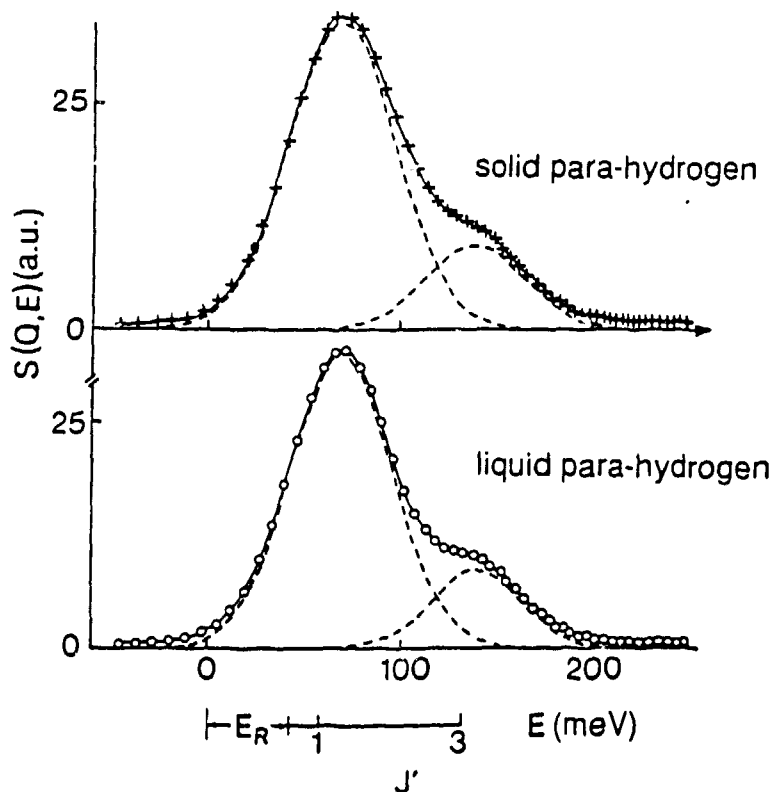


Fig. 9 The observed scattering from liquid and solid para-hydrogen. The crosses are the experimental results. The dashed lines are the predicted IA scattering from the hydrogen molecule when the  $J=0$  to  $J=1$  (14.7 meV) and  $J=0$  to  $J=3$  (88.2 meV) rotational transitions are excited (from ref 47).

The situation is similar in nuclear physics. Fig. 10 shows an overview of the nuclear response function. The resemblance to Fig. 8 for the atomic case is striking. At low  $Q$  and  $\omega$ , nuclear response is dominated by elastic scattering, by inelastic scattering to low-lying states, and by collective excitations such as the giant resonances. At higher momentum and energy transfers the scattering is described essentially by the impulse approximation (region II).  $Y$ -scaling applies only in this region. At even higher momentum and energy transfers, nucleonic excitation and particle creation break the scaling behavior. Finally, at extremely high energies scaling behavior of a different sort, associated with electron scattering from the quark constituents of the nucleon, sets in. (For further details on deep-inelastic scattering from nucleons and “ $x$ -scaling,” see the article by West in these proceedings.<sup>29</sup> )

As an example of scale breaking in nuclear physics, refer once again to the measurements on  $^{12}\text{C}$  plotted in Fig. 6. At low momentum transfers, the quasielastic scattering can be described by  $Y_S$  scaling up to  $Y_S \approx -0.1 \text{ GeV}/c$  or so. However, as the incident energy is increased, more energy is available to create internal excitations and  $Y$ -scaling breaks down at lower and lower values of  $Y_S$ . This is exactly analogous to what is seen in neutron scattering from molecular hydrogen.

We emphasize that scale-breaking phenomena have nothing to do with the break-

breaking (as the term is conventionally understood) is due to the excitation of internal degrees of freedom of constituent particles. In principle, momentum distributions could still be determined in the presence of scale breaking by inverting a more general impulse-approximation formula, such as eq. (5.12) or eq. (5.17). However, this has yet to be attempted in practice.

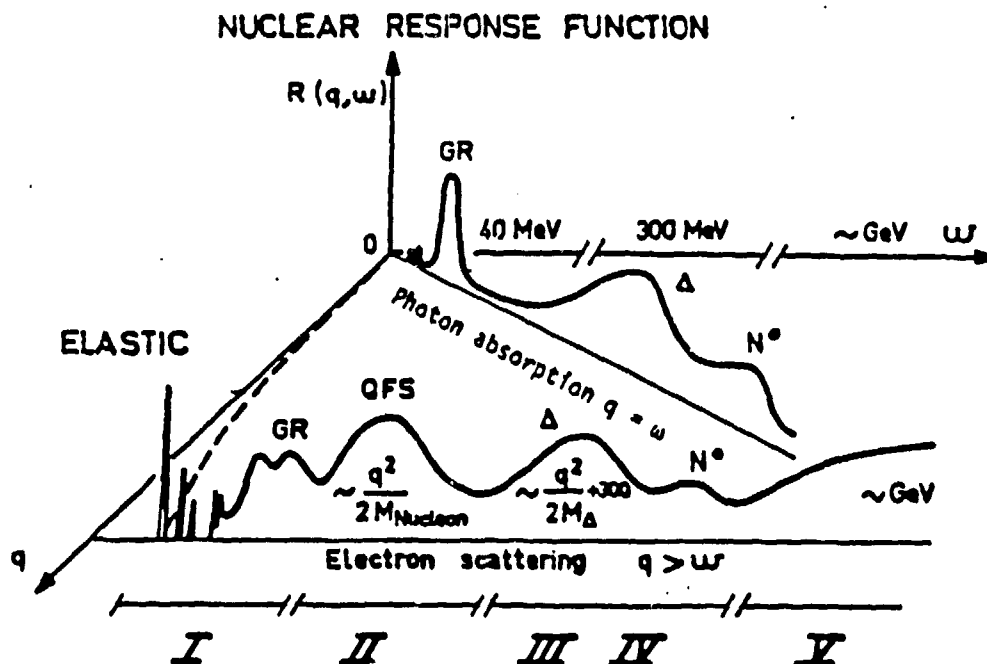


Fig. 10 Schematic of the nuclear response function  $R(Q, \omega)$  as a function of energy and momentum transfer. The scattering at low energies (region I) is dominated by the elastic peak and inelastic scattering from low-lying states and the giant resonances (GR). At slightly higher energy transfers (region II) *quasifree scattering* (QFS) from nucleons initially bound in the nuclear medium is observed. This is the region where the momentum distribution of the nucleons is accessible using QENS. At larger energy transfers (region III-IV) sufficient energy is available to create pions and to excite the nucleon ( $\Delta$ ,  $N^*$ , resonances, etc.). Finally, at very large energy and momentum transfers (region V), electrons are scattered directly from the quark constituents of the nucleons (from ref 48).

#### Limitations on Determining $n(p)$

The impulse approximation provides a simple relationship between the single-particle momentum distribution,  $n(p)$ , and the observed scattering expressed in terms of a Compton profile,  $J(Y)$ . The experimental goal is to extract the momentum distribution from scattering measurements. Unfortunately, the extraction is hampered by the fact that prominent – and physically interesting – features in  $n(p)$  may not be strongly reflected in  $J(Y)$ , due to the integral form of the impulse-approximation relationship (cf. eqs. (5.7), (5.8), (5.12), and (5.17)).

To illustrate this fact, consider the ground-state momentum distribution of liquid  $^4\text{He}$ . Fig. 11a shows the results of two different microscopic calculations, based on GFMC<sup>24</sup> and variational<sup>49</sup> (HNC/S) techniques. In both cases,  $n(p)$  has a delta function at  $p = 0$  representing the Bose condensate, with condensate fraction  $n_0 = 0.2$

they differ markedly at small but finite  $p$ . The variational calculation reproduces the  $p^{-1}$  singular behavior at small  $p$  which is due to coupling of long-wavelength density fluctuations to the condensate. On the other hand, the GFMC result for  $n(p)$  shows no sign of this singularity, because of the finite size of the simulation box. Thus, while the two results for  $n(p)$  are palpably different, the corresponding  $J(Y)$  curves generated by the impulse approximation (Fig. 11b) differ only very slightly. When the respective impulse-approximation results for  $J(Y)$  are in turn broadened by the final-state effects given by Silver's theory<sup>43</sup> (Fig. 11c), the predictions corresponding to the two microscopic calculations become indistinguishable. We conclude that the scattering experiment is insensitive to the singular behavior of  $n(p)$  at small  $p$  which accompanies a proper treatment of long-range correlations. This insensitivity is obviously due to the fact that, in the isotropic case,  $J(Y)$  reduces to an integral over  $pn(p)$ .

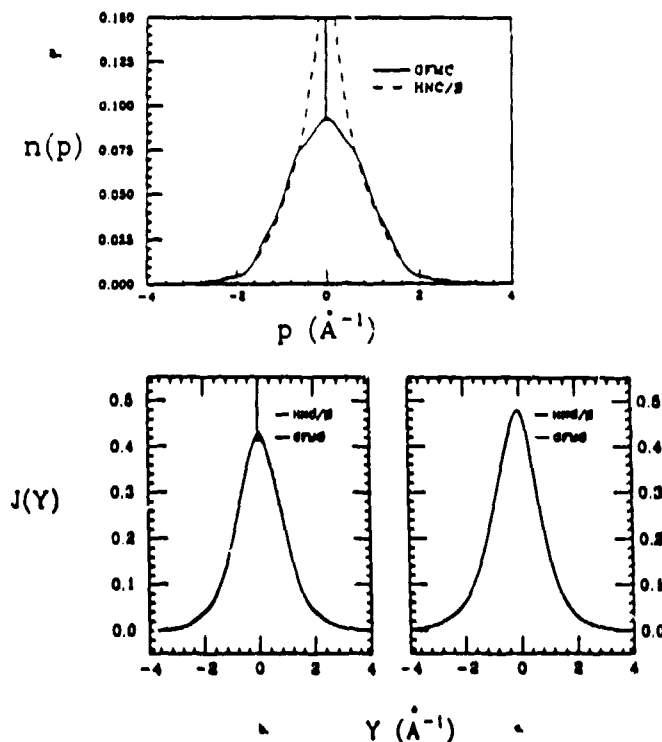


Fig. 11 Illustration of the relationship between  $n(p)$  and  $J(Y)$ . a) shows the results of GFMC<sup>24</sup> (solid curve) and variational<sup>49</sup> (dashed curve) calculations of  $n(p)$  in the ground state of liquid  $^4\text{He}$ . Both calculations predict a condensate fraction of 10 % which gives a  $\delta$ -function at  $p = 0$  (not visible in the variational calculation). In addition, the variational calculation predicts a singular behavior at small  $p$  which is absent in the GFMC result. b) shows the effect of transforming  $n(p)$  to  $J(Y)$  using (5.7). The  $\delta$ -function is still present. However, the singular behavior, which is the dominant feature in the variational  $n(p)$  at small  $p$ , is now much less prominent. c) shows the results of including the final state broadening shown in Fig. 7. The two curves are now nearly indistinguishable.

The above comparison documents an important limitation on the ability to extract information on the momentum distribution from scattering measurements. The physically measured quantity is the Compton profile  $J(Y)$ , not the momentum distribution  $n(p)$ . While, in principle,  $n(p)$  could be obtained by numerical differentiation of  $J(Y)$  data, it is clear that excellent statistics – perhaps unattainable in practice – would be required to distinguish experimentally between the two microscopic calculations for  $n(p)$ .

To round out this overview we present a few examples of momentum distributions in atomic, electronic, and nuclear systems. We give a sampling of both theoretical and experimental results, obtained both for classical systems, where statistics do not play a significant role, and for quantum systems, where they do.

### *Classical Systems*

In atomic systems we encounter numerous examples in which the momentum distribution assumes the classical Maxwell-Boltzmann form. Except for the lighter elements, such as helium and hydrogen, the quantum nature of the constituent atoms plays a minor or insignificant role in the momentum distribution. In general, the interactions between the atoms are relatively strong, whereas zero-point motion is small. Accordingly, there is little overlap of the atomic wave functions in the condensed phases, which means that exchange effects are unimportant. Then it is an excellent approximation to treat the atomic 'particles' classically, with quantum effects included perturbatively as required.

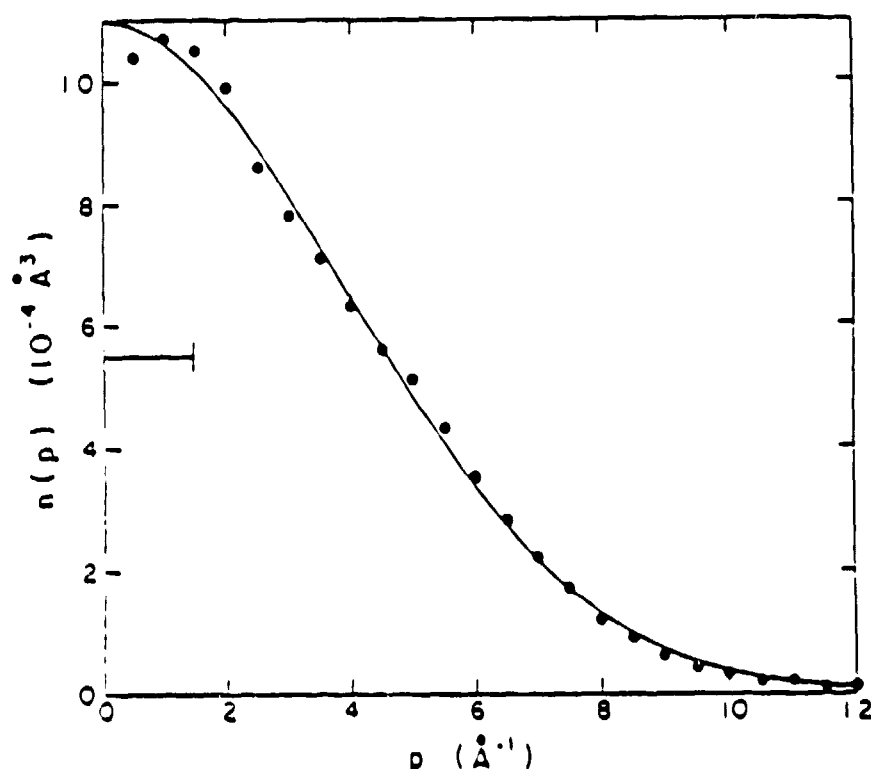


Fig. 12 The normalized momentum distribution for liquid neon at  $T=29.6$  K. The dots are the experimental results. The solid line is a Gaussian, the classical form for  $n(p)$ , with the same root-mean-square momentum (from ref 50).

Fig. 12 depicts the momentum distribution of liquid neon at 29.6 K, as inferred from inelastic neutron-scattering measurements.<sup>50</sup> The scattering results are well described in terms of a simple Gaussian form for  $n(p)$ , in accord with the classical prediction. For given particle mass, the width of the classical momentum distribution is determined by the temperature of the system. The average kinetic energy per atom, which is proportional to the width of the momentum distribution, is then expected to have the familiar ideal-gas value  $3k_B T/2$ . The kinetic energy extracted from the inferred momentum distribution for neon is 48.2 K, which is somewhat higher than the expected value of 44.4 K.

The differences between the measured and expected kinetic energies for neon can be attributed to quantum effects. These are small, although observable because neon

such as argon, krypton, and xenon. The principal correction to the classical result comes from the small zero-point motion of the atoms. When this effect is small, corrections of increasing order may be made using the series

$$\langle K \rangle = \frac{3}{2} k_B T \left( 1 + \frac{1}{12} (\theta/T)^2 - \frac{1}{240} (\theta/T)^4 + \dots \right), \quad (6.1)$$

where  $\theta^2 = (\hbar^2/3mk^2) \langle \Delta\Phi \rangle$ . The quantity  $\Delta\Phi$  is the Laplacian of the potential energy. In the solid phase, the form of the corrections for zero-point motion is very similar, the role of  $\theta$  being played by the Debye temperature,  $\theta_D$ . Returning to the comparison of kinetic energies for liquid neon and incorporating the quantum zero-point correction, one obtains a theoretical prediction for the kinetic energy of 49.5 K, considerably improving the agreement with the measured kinetic energy.

### *Bose Systems*

Liquid  $^4\text{He}$  provides the most celebrated example in which the Bose character of the constituent particles has a crucial influence on the properties of the many-body system, and especially on its momentum distribution. The interatomic potential in helium has a weak attractive portion and a condensed liquid phase does not form, at vapor pressure, until the temperature is decreased to 4.2 K. Indeed, the interactions are so weak that the system remains in a liquid phase down to zero temperature, when no external pressure is applied. Due to the weak attractive interactions and the light mass of the helium atom, the quantum zero-point motion is very large in the liquid. This implies a very large overlap of atomic wave functions naively proposed to describe the system. Correspondingly, exchange effects are expected to be very important.

The high temperature properties of liquid helium are similar to those of conventional liquids. However, when the temperature is lowered to about 2.2 K there occurs a phase transition from liquid helium I to a new phase, liquid helium II. The transition is signaled by a sharp feature in the specific heat – the famous  $\lambda$ -point anomaly. Liquid helium II, often called the superfluid phase, appears to contain a superfluid component which flows without viscosity and is responsible for an anomalously large thermal conductivity. Normal dissipative effects are attributed to a normal-fluid component. According to this “two-fluid model,” the fraction of superfluid increases to unity at absolute zero. The success of the phenomenological two-fluid picture is thought to be indicative of the appearance of a Bose condensate in the momentum distribution,<sup>51</sup> a manifestation of Bose statistics with striking macroscopic repercussions. There has been a forty-year history of attempts to observe this Bose condensate by neutron scattering experiments.<sup>52</sup>

Fig. 13a shows the measured scattering,  $J(Y)$ , in the normal liquid phase (liquid He I) at 3.5 K, where no condensate is present. Theoretical predictions for the scattering are drawn as solid and dashed lines. The momentum distribution, calculated using the PIMC method,<sup>26</sup> is nearly Gaussian at helium II temperatures and has been converted to  $J(Y)$  via the impulse-approximation (IA) formula. To allow direct comparison with experimental data, this prediction for  $J(Y)$  has been artificially broadened using a model of the instrumental resolution, resulting in the dashed curve. The agreement is excellent. The significance of the solid curve will be explained below.

Fig. 13b shows the measured scattering in the superfluid phase (liquid He II) at 0.35 K. The dashed line is again an instrumentally-broadened theoretical prediction based on the IA formula, this time using as input the  $n(p)$  from a ground-state GFM calculation<sup>24</sup> which yields a condensate fraction of 9.2 %. Due to the instrumental broadening, the IA prediction no longer exhibits a distinct condensate peak. However, it retains a sharper peaking around  $Y = 0$  than in the normal liquid, which

too large an intensity around  $Y = 0$  and is in generally poor agreement with the observed scattering.

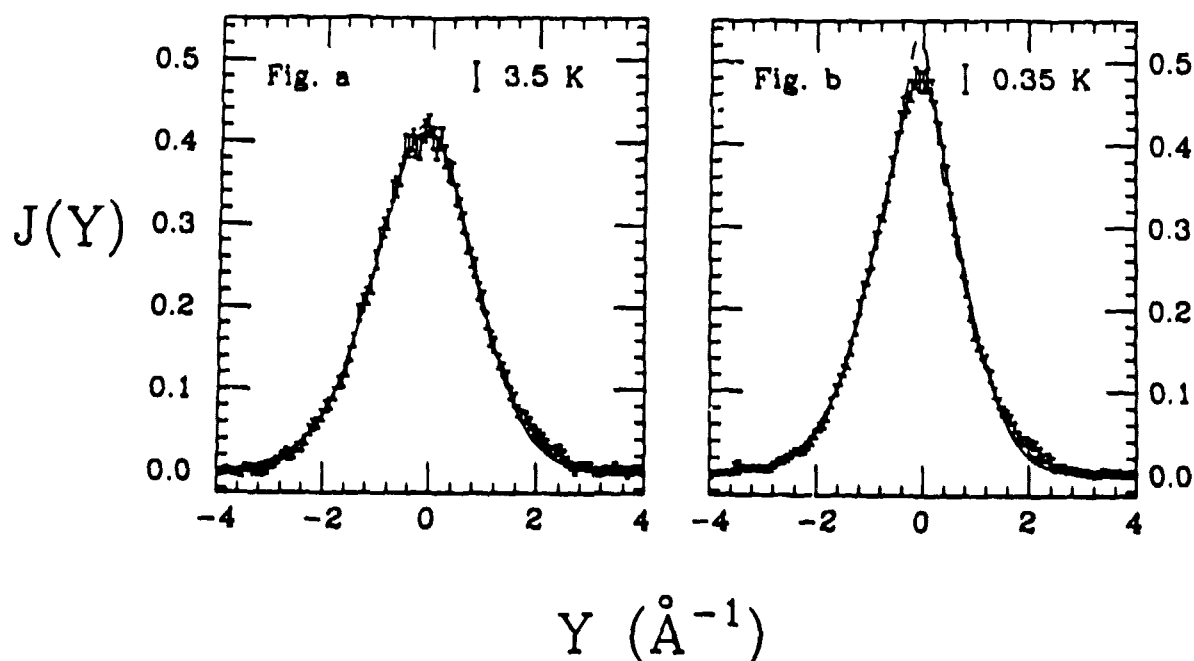


Fig. 13 The measured scattering in the normal liquid phase at 3.5 K (a) and the superfluid phase at 0.35 K (b) of liquid  $^4\text{He}$ . The dashed curves are the theoretical predictions for  $n(p)$  transformed to  $J(Y)$  and convoluted with instrumental resolution. PIMC<sup>26</sup> calculations at 3.33 K have been used for comparison with the normal liquid and are in excellent agreement with the experimental results. GFMC<sup>24</sup> calculations have been used for comparison with the superfluid and large discrepancies exist near  $Y = 0$ . The solid curves are again the theoretical predictions, but including the FSE broadening shown in Fig. 7. The agreement between theory and experiment is now excellent in both the normal and superfluid phases (from ref 53).

The results of this comparison in the superfluid phase could be interpreted as an indication that the condensate fraction is far smaller than theoretically predicted. However, such an inference is unjustified without a consideration of the final-state broadening of the condensate peak. We may take final-state effects into account by convoluting the instrumentally-broadened IA result with a final-state broadening function furnished by the recent theory of Silver<sup>43</sup> (Fig. 7). In the normal-liquid case (Fig. 13a), this produces the solid curve, which is indistinguishable from the predicted scattering without final-state effects. Thus, final-state interactions have little effect in the presence of the broad momentum distribution of the normal liquid.

Turning to the superfluid case, the solid curve in Fig. 13b gives the theoretically predicted scattering when final-state broadening as well as instrumental resolution is incorporated. There is now striking agreement with the experimental data! This analysis provides a dramatic example of the importance of final-state broadening when a sharp feature is present in the momentum distribution. Moreover, the excellent agreement between theory and experiment furnishes strong support for the existence of a condensate in the superfluid and for the validity of the microscopic calculations of the momentum distribution.

Examples in which the Fermi character of the constituent particles is strongly reflected in  $n(p)$  are quite widespread and can be found in atomic, electronic, and nuclear systems.

Fig. 14a displays the results of some representative microscopic calculations of the momentum distribution of the interacting electron gas (one-component plasma), at a density pertinent to sodium. The solid line is from a variational calculation based on an optimal Jastrow wave function,<sup>54</sup> which accounts, in an average way, for the effects of both short-range and long-range correlations. The long- and short-dashed lines correspond to older 'perturbative' calculations,<sup>55</sup> which invoke the random-phase approximation and thus concentrate (in a more detailed manner) on the long-range correlations. The momentum distribution of the noninteracting Fermi gas is also plotted for reference.

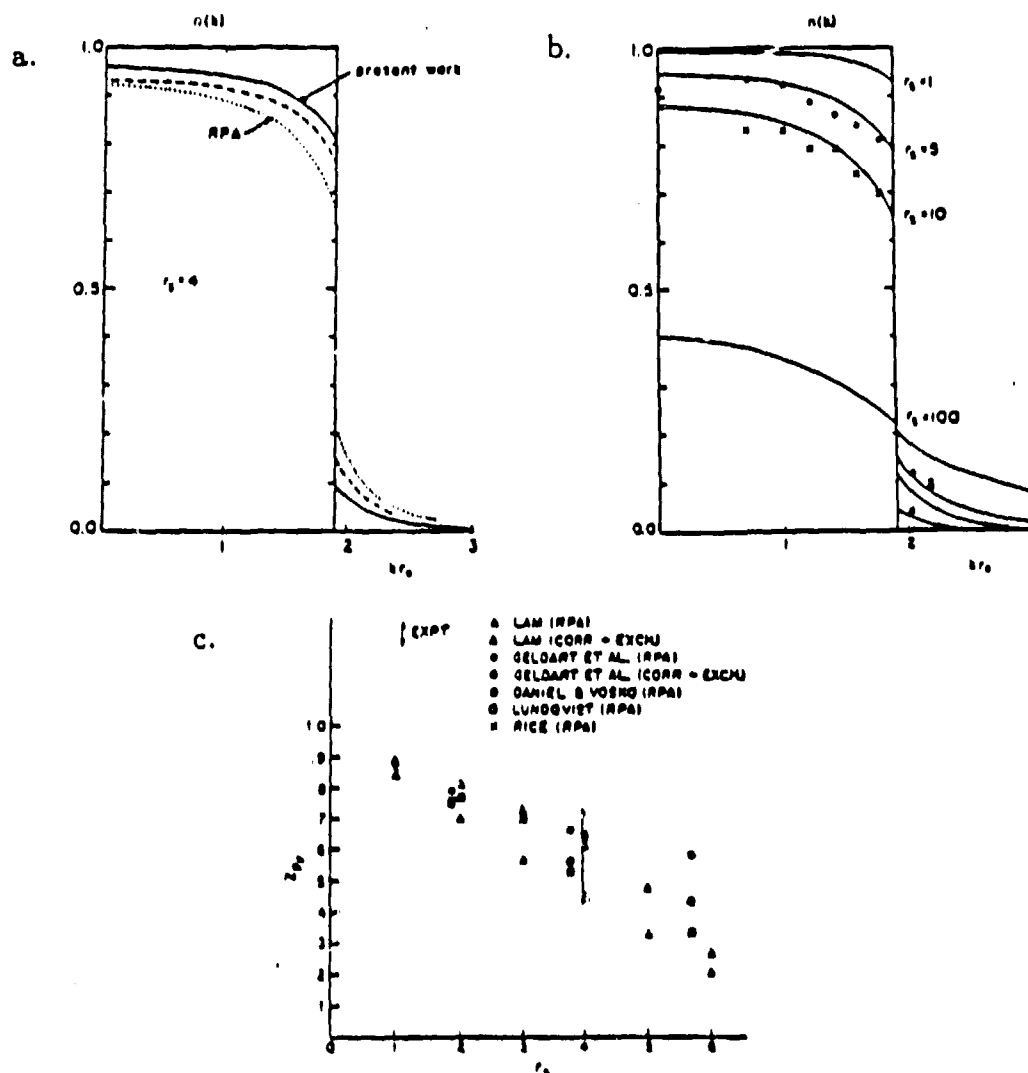


Fig. 14 Theoretical calculations of  $n(p)$  for the interacting electron gas. a)  $n(p)$  at a density comparable to Na. The solid line is a variational calculation and the dashed lines are perturbative calculations.  $n(p)$  for the noninteracting Fermi gas is also shown for reference (from ref 54). b) Density dependence of  $n(p)$ . The curves are variational calculations of  $n(p)$  and the open circles and crosses are Monte Carlo results. Smaller values of  $r_s$  correspond to higher density for the interacting electron gas (from ref 54). c) Theoretical results for the discontinuity  $Z$  of the homogeneous electron gas as a function of density. The experimental results for metallic Na are included for comparison (from ref 57).



electronic density, smaller  $r_s$ , corresponding to higher density. The two densities considered differ by a factor  $2^{1/3}$ . The curves were obtained by the same optimal Jastrow treatment which gave the solid line in Fig. 14a, the required expectation values being evaluated in a hypernetted-chain approximation which neglects elementary diagrams.<sup>54</sup> The dots show the results of comparable variational Monte Carlo calculations,<sup>56</sup> which attest to the validity of this approximation. We observe that the discontinuity  $Z_{k_F}$  of  $n(p)$  at the Fermi surface narrows as the density decreases, which implies that the system is becoming more strongly coupled. This behavior is due to the fact that the screening of the long-range coulombic interaction between the electrons becomes less effective at lower density. The contrary behavior is seen in the atomic (viz. liquid  $^3\text{He}$ ) and nuclear cases, where the basic interactions are of short range and  $Z$  decreases as the density increases.

Fig. 14c collects a variety of theoretical results for the discontinuity  $Z$ , or "quasi-particle pole strength," of the homogeneous electron gas, and indicates that this system can display a range of behaviors between weak and strong coupling, in the density regime relevant to alkali metals. The result of an experimental determination of  $Z$  for metallic Na is included for comparison.<sup>57</sup>

Fig. 15 sketches the momentum distributions obtained in a recent theoretical study of nuclear matter within the method of correlated basis functions.<sup>58</sup> These results document the importance of the tensor interaction in depleting the Fermi sea. With tensor forces present, the Fermi surface discontinuity is  $Z \sim 0.7$ , very close to that found in the optimal Jastrow calculation for the uniform electron gas at the density corresponding to metallic Na. In this sense, nuclear matter and the electron gas may be considered as comparably strongly interacting. Omitting the tensor component of the nucleon-nucleon potential, the nuclear-matter  $Z$  increases to about 0.85. In finite nuclei, the Fermi-surface discontinuity is broadened.

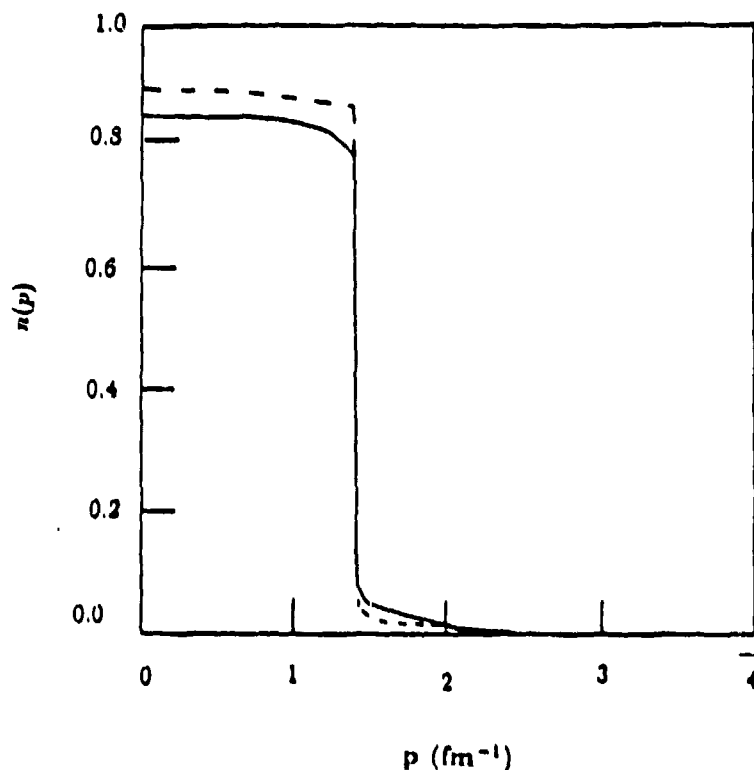


Fig. 15 Momentum distribution in nuclear matter using the method of correlated basis functions. The solid curve includes the tensor component of the nucleon-nucleon potential, while the dashed curve shows the effect of omitting this component (adapted from ref 58).

momentum distribution in liquid  $^3\text{He}$  at  $T = 0$ . The fixed-node GPMC calculation<sup>24</sup> and the variational treatment labeled FHNC<sup>59</sup> predict essentially the same results for  $n(p)$ . There is a Fermi-surface discontinuity of roughly 0.3 (not resolved in the GPMC evaluation). This small value supports the view that liquid  $^3\text{He}$  is the most strongly interacting of the Fermi systems we have considered. The FHNC variational treatment is predicated on a conventional trial ground-state wave function including Jastrow two-body correlations, triplets, and backflow; it makes use of "scaling" and cluster-expansion procedures in addition to Fermi-hypernetted-chain (FHNC) resummation.

By contrast, the variational Monte Carlo calculation of Bouchaud and Lhuillier,<sup>60</sup> assumes a radically different trial wave function for the  $^3\text{He}$  ground state, incorporating odd-wave pairing correlations as well as a Jastrow factor. This departure from tradition has a dramatic consequence for  $n(p)$ : the Fermi surface disappears entirely. The implications of the Bouchaud-Lhuillier work are yet to be fully explored, but it suggests that there is still room for improvement in our fundamental understanding of liquid  $^3\text{He}$ , which serves as a prototype for testing approaches to other strongly-correlated Fermi systems.

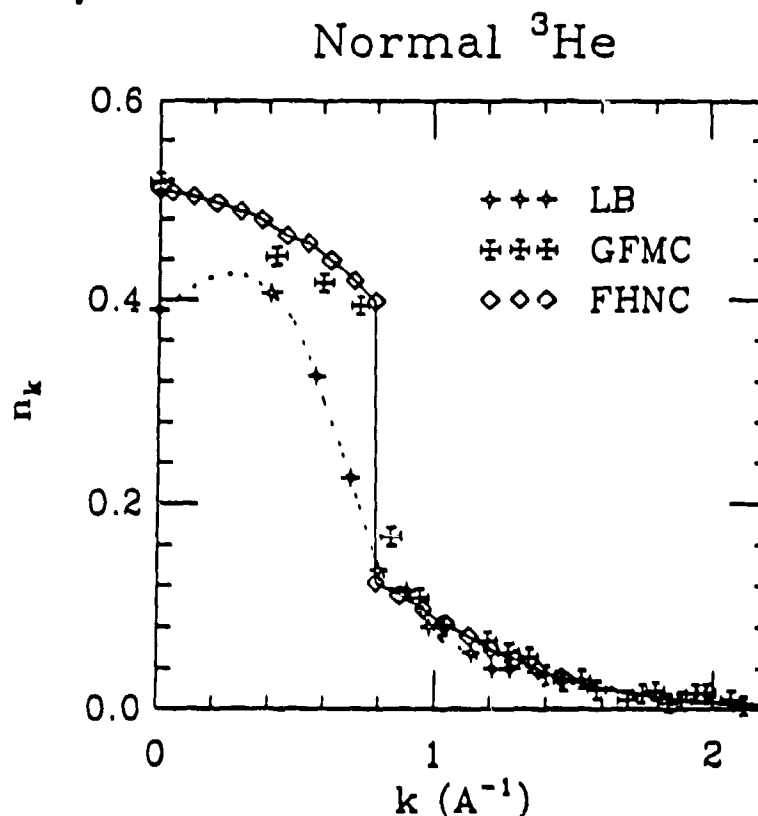


Fig. 16 Theoretical  $n(p)$  for liquid  $^3\text{He}$ . The FHNC<sup>59</sup> and GPMC<sup>24</sup> calculations yield very similar predictions for  $n(p)$  with a Fermi-surface discontinuity of roughly 0.3. The Bouchaud and Lhuillier<sup>60</sup> (BL) calculation, which uses a radically different trial wave function incorporating odd-wave pairing, predicts that the Fermi-surface disappears entirely.

## CONCLUSION

We hope that this overview has convinced readers that momentum distributions are fundamental to our understanding of quantum many-body systems in most areas of physics. Even though the energy and length scales vary by more than ten orders of magnitude, we have identified common conceptual and methodological elements in theoretical and experimental studies of atomic, electronic, and nuclear systems. For lack of space, our overview has not developed upon the similar analogies which

trial wells such as metal hydrides,<sup>62,63</sup> and positron-annihilation studies of electronic systems.<sup>7</sup> Nor have we discussed momentum-distribution experiments in which more than one outgoing particle is detected.

Recently, there have been impressive advances in the theoretical calculation of momentum distributions. Numerical calculations, using GFMC and PIMC techniques, have benefited greatly from the accessibility of supercomputers and are beginning to provide extremely accurate descriptions of the momentum distribution. In addition, there have been significant conceptual improvements in the variational wave functions used to describe many-body systems. Moreover, the number of strongly-interacting many-body systems for which momentum distributions are of interest is expanding rapidly, particularly with the discoveries of strongly-correlated electronic systems such as the heavy-fermion materials, high-temperature superconductors, and structures displaying quantum Hall effects.<sup>8</sup> Accompanying these discoveries is an expanding variety of possibilities for variational wave functions of Fermi systems.

We have also discussed recent theoretical advances in the calculation of corrections to the impulse approximation due to final-state effects in atomic and nuclear systems. These effects can be quite important since they cannot be experimentally eliminated in feasible experiments on atomic and nuclear systems. We have shown that a quantitative theoretical characterization is essential to the detailed interpretation of the experimental results.

There have also been impressive advances on the experimental side. The development of new sources with increased energy and flux is expanding both the range of systems that can be studied and the amount of detailed information that can be obtained. Spallation neutron sources, such as IPNS, ISIS, and LANSCE, provide much larger fluxes at higher energies than were hitherto attainable. Synchrotron sources offer many orders of magnitude greater flux than available in laboratory X-ray facilities, and they have stimulated a revival of Compton-scattering experiments. New synchrotron sources, such as the Advanced Photon Source with special insertion devices including wigglers and undulators, will further enhance the capabilities for this class of measurement by several more orders of magnitude, and in particular they will facilitate the measurement of magnetic Compton profiles. New positron facilities and imaging capability should yield enormous improvements in studies of the Fermi surface of electronic systems. New facilities for nuclear physics research, such as CEBAF, will furnish much higher intensities for electron-scattering studies of nuclei and will facilitate the exploration of high-momentum components of the nuclear wave function. One can only imagine what momentum-distribution studies will become possible with the 20 TeV energies of the Superconducting Super Collider, or what constituent particles will form the basis for the impulse approximation (Higgs bosons?). Accompanying the development of these new, more intense and higher energy sources is the development of new and improved instrumentation with much better resolution. Most of these technical advances are discussed in more detail elsewhere in this volume.

In conclusion, we are now poised for an explosive growth of knowledge within the next few years about momentum distributions in many-body systems in all areas of physics. It is our conviction that this progress will benefit greatly from an interdisciplinary sharing of concepts and methodology, which has motivated the organization of this workshop. Our investigations of momentum distributions have convinced us, once again, of the essential unity of physics.

The following research support is acknowledged. PES: NSF Grant No. DMR-8704288; OBES/DMS support of the Intense Pulsed Neutron Source at Argonne National Laboratory under DOE grant W-31-109-ENG-38. RNS: OBES/DMS support of the Los Alamos Neutron Scattering Center at the Los Alamos National Laboratory. JWC: Condensed Matter Theory Program of the Division of Materials Research, National Science Foundation, under Grant No. DMR-8519077.

- 1 B. Williams, **Compton Scattering**, (Mc Graw Hill, 1977).
- 2 A. N. Antonov, P. E. Hodgson, I. Zh. Petkov, **Nucleon Momentum and Density Distributions in Nuclei**, (Clarendon Press - Oxford, 1988).
- 3 J. Gavoret and P. Nozières, *Ann. Phys. (N. Y.)* **B28**, 349 (1964).
- 4 O. Penrose and L. Onsager, *Phys. Rev.* **B104**, 576 (1956).
- 5 C. N. Yang, *Rev. Mod. Phys.* **B34**, 694 (1962).
- 6 J. Clark and M. Ristig, contribution at this conference.
- 7 S. Berko, contribution at this conference.
- 8 S. Doniach, contribution at this conference.
- 9 K.A. Brueckner, *Phys. Rev.* **97**, 1353 (1955); **100**, 36 (1957).
- 10 J. Goldstone, *Proc. Roy. Soc. (London)* **A239**, 267 (1957).
- 11 B.D. Day, *Rev. Mod. Phys.* **39**, 719 (1967).
- 12 A. B. Migdal, *Soviet Phys.-JETP* **B5**, 333 (1957).
- 13 J. M. Luttinger, *Phys. Rev.* **B119**, 1153 (1960).
- 14 A. D. Jackson, A. Lande, and R. A. Smith, *Physics Reports* **B86**, 55 (1982).
- 15 R.B. Laughlin, *Phys. Rev. Lett.* **50**, 1395 (1983); *Surf. Sci.* **142**, 163 (1984).
- 16 J. M. Chen, J. W. Clark, and D. G. Sandler, *Z. Phys. A* **B305**, 223 (1982).
- 17 E. Krotscheck, *Phys. Rev. A* **B26**, 3536 (1982).
- 18 G. Senger, M. L. Ristig, K. E. Kurten, and C. E. Campbell, *Phys. Rev.* **B33**, 7562 (1986).
- 19 Q. N. Usmani, B. Friedman, and V. R. Pandharipande, *Phys. Rev.* **B25**, 4502 (1982); Q. N. Usmani, S. Fantoni, and V. R. Pandharipande, *Phys. Rev.* **B26**, 6123 (1982); M. F. Flynn, *Phys. Rev.* **B33**, 91 (1986).
- 20 A. Fabrocini and S. Rosati, *Nuovo Cimento* **BD1**, 567, 615 (1982); M. Viviani, E. Buendia, A. Fabrocini, and S. Rosati, *Nuovo Cimento* **BD8**, 561 (1986).
- 21 S. Vitiello, K. Runge, and M.H. Kalos, *Phys. Rev. Lett.* **60**, 1970 (1988).
- 22 E. Feenberg, **Theory of Quantum Fluids** (Academic, New York, 1969).
- 23 J.W. Clark and P. Westhaus, *Phys. Rev.* **141**, 833 (1966).
- 24 P. Whitlock and R. M. Panoff, *Can. J. Phys.* **B65**, 1409 (1987).
- 25 R.M. Panoff and J. Carlson, *Phys. Rev. Lett.* **62**, 1130 (1989).
- 26 D.M. Ceperley and E.L. Pollock, *Phys. Rev. Lett.* **56**, 351 (1986).
- 27 A.H. Compton, *Phys. Rev.* **21**, 207 (1923); **21**, 483, (1923).
- 28 For a history, see the article by R.H. Stuewer and M. J. Cooper in reference 1.
- 29 G. West, contribution at this conference.
- 30 G.L. Squires **Introduction to the Theory of Thermal Neutron Scattering** (Cambridge University Press, 1978).
- 31 Note, that for the purposes of this discussion we have used a non-standard definition of the coherent structure factor.
- 32 G. Reiter and R. Silver, *Phys. Rev. Lett.* **54**, 1047 (1985).
- 33 P.C. Hohenberg and P.M. Platzman, *Phys. Rev.* **152**, 198 (1966).
- 34 G.B. West, *Phys. Rep.* **18C**, 263 (1975).
- 35 J. Weinstein and J. W. Negele, *Phys. Rev. Lett.* **49**, 1016 (1982).
- 36 R. N. Silver and G. Reiter, *Phys. Rev.* **B35**, 3647 (1987).
- 37 W. Clark and R. N. Silver, *Proceedings of the Vth International Conference on Nuclear Reaction Mechanisms, Varenna, Italy 1988* from data taken by T. R. Sosnick, W. M. Snow, P. E. Sokol, R. N. Silver, to be published, and W. G. Stirling, E. F. Talbot, B. Tanatar, H. R. Glyde, to be published
- 38 J. W. M. Du Mond, *Phys. Rev.* **33**, 643 (1925).
- 39 I. Sick, D. Day, and J. S. McCarthy, *Phys. Rev. Lett.* **45**, 871 (1980).
- 40 D. B. Day *et al.*, *Phys. Rev. Lett.* **59**, 427 (1987).
- 41 I. Sick, *Comments Nucl. Part. Phys.* **18**, 109 (1988).
- 42 P.E. Sokol, T.R. Sosnick, W.M. Snow, and R.N. Silver, contribution at this conference.

- 45 P.E. Sokol, contribution at this conference.
- 46 R.O. Simmons and P.E. Sokol, *Physica* **136B**, 156, 1986.
- 47 W. Langel, D. L. Price, R. O. Simmons, and P. E. Sokol, *Phys. Rev.* **B38**, 11275 (1988).
- 48 B. Frois in *Progress in Particle and Nuclear Physics* , Vol 13, ed. A. Faessler.
- 49 E. Manousakis, V. R. Pandharipande, and Q. N. Usmani, *Phys. Rev.* **B31**, 7022 (1985).
- 50 V.F. Sears, *Can. J. Phys.* **59**, 555 (1981).
- 51 F. London, *Nature* **141**, 643 (1938).
- 52 for reviews see e.g. E.C. Svensson, V.F. Sears, *Physics* **137B**, 126 (1986).
- 53 T.R. Sosnick, W.M. Snow, and P.E. Sokol, to be published.
- 54 L. J. Lantto, *Phys. Rev.* **B22**, 1380 (1980).
- 55 J. Lam, *Phys. Rev.* **B3** , 3243 (1971).
- 56 D. Ceperley, unpublished.
- 57 P. Eisenberger, L. Lam, P. M. Platzman, and P. Schmidt, *Phys. Rev.* **B6**, 3671 (1972); and references therein.
- 58 S. Fantoni and V. R. Pandharipande, *Nucl. Phys.* **BA427**, 473 (1984).
- 59 A. Fabrocini, V. R. Pandharipande, and Q. N. Usmani, to be published.
- 60 J. P. Bouchaud and C. Lhuillier, *Europhys. Lett.* **B3**, 1273 (1987).
- 61 I. McCarthy, in *High Energy Excitations in Condensed Matter*. LASL Report No. LA-10227-Z, Los Alamos National Laboratory, NM.
- 62 G. Reiter, contribution at this conference.
- 63 D.L. Price and R. Hempleman, contribution at this conference.